REPORT DOCUMENTATION PAGE

Form Approved OMB No. 0704-0188

1. REPORT DATE *(DD-MM-YYYY)*	2. REPORT TYPE	3. DATES COVERED *(From - To)*
05-01-2011	Final Technical	01-06-2007 - 31-12-2010

4. TITLE AND SUBTITLE

(YIP) Mid-Infrared Laser Absorption Diagnostics for Combustion and Propulsion Applications

5a. CONTRACT NUMBER

5b. GRANT NUMBER
N00014-07-1-0844

5c. PROGRAM ELEMENT NUMBER

6. AUTHOR(S)

Matthew A. Oehlschlaeger

5d. PROJECT NUMBER

5e. TASK NUMBER

5f. WORK UNIT NUMBER

7. PERFORMING ORGANIZATION NAME(S) AND ADDRESS(ES)

Rensselaer Polytechnic Institute
Mechancial, Aerospace, and Nuclear Engineering Dept
Troy NY 12180-3590

8. PERFORMING ORGANIZATION REPORT NUMBER

9. SPONSORING / MONITORING AGENCY NAME(S) AND ADDRESS(ES)
Dr. Gabriel D. Roy
Office of Naval Research
875 North Randolph Street
Arlington, VA 22203-1995

10. SPONSOR/MONITOR'S ACRONYM(S)

11. SPONSOR/MONITOR'S REPORT NUMBER(S)

12. DISTRIBUTION / AVAILABILITY STATEMENT

Approved for public release. Distribution is unlimited.

13. SUPPLEMENTARY NOTES

14. ABSTRACT

The objective of the present research program was to develop mid-infrared (mid-IR) laser absorption sensors based on quantum cascade laser (QCL) technology for combustion and propulsion applications. To demonstrate the potential of mid-IR QCL absorption sensors for sensitive and selective measurements of temperature and species concentrations, a carbon monoxide (CO) and thermometry sensor was developed which probes several CO transitions around a wavelength of 4.59 microns. The sensor was demonstrated in a static gas cell, in shock-heated gases, and in a flat flame at conditions ranging from room temperature to 3500 K, sub-atmospheric to five atmospheres of total pressure, and for mixtures containing 10s of ppms to 10% CO. Sensor thermometry and CO concentration determinations are shown to typically deviate by 1-2% with expected values. At room temperature and one atmosphere of pressure, CO detection limits are 30-400 ppb per meter of absorption path length for a detection bandwidth of 1 kHz.

15. SUBJECT TERMS

Laser diagnostics, laser sensors, mid-infrared (mid-IR), quantum cascade laser (QCL), absorption, wavelength modulation, thermometry, temperature measurement, carbon monoxide (CO)

16. SECURITY CLASSIFICATION OF:			17. LIMITATION OF ABSTRACT	18. NUMBER OF PAGES	19a. NAME OF RESPONSIBLE PERSON
a. REPORT	b. ABSTRACT	c. THIS PAGE			Dr. Gabriel D. Roy
Unclassified	Unclassified	Unclassified	UL	53	19b. TELEPHONE NUMBER *(include area code)* 703-696-4406

Mid-Infrared Laser Absorption Diagnostics for Combustion and Propulsion Applications

Prepared Under
Grant # N00014-07-1-0844

Final report submitted by:
Matthew Oehlschlaeger, Ph.D. (PI)
Rensselaer Polytechnic Institute
Mechanical, Aerospace, and Nuclear Engineering Department
110 8th St.
Troy, NY 12180

Submitted to:
Dr. Gabriel D. Roy
Office of Naval Research
875 N. Randolph St.
Arlington, VA 22203-1995

For the period:
June 1, 2007 – December 31, 2010

Contents

1. Executive Summary 3
2. Introduction 4
3. Theory and Line Selection 6
   3.1. Direct Absorption 6
   3.2. Wavelength Modulation Spectroscopy 10
4. Sensor Architecture and Operation 12
5. Scanned-Wavelength Direct-Absorption Sensor Demonstrations 16
   5.1. Low-Temperature Gas Cell Measurements 16
   5.2. High-Temperature Shock Tube Measurements 20
   5.3. Flat Flame Measurements 26
6. Wavelength-Modulation Sensor Demonstrations 31
   6.1. Low-Temperature Gas Cell Measurements 31
   6.2 High-Temperature Shock Tube Measurements 33
7. Summary 35
8. Participating Personnel 36
9. Publications 36
10. References 36
A. Appendix: The Photo-Ignition of Quiescent Fuel/Air Mixtures Containing Suspended Carbon Nanotubes 38
   A.1. Introduction 38
   A.2. Experimental Method 41
   A.3. Results and Discussion 45
   A.4. Summary 52
   A.5. References 52

1. Executive Summary

Mid-infrared (mid-IR) laser absorption sensors based on quantum cascade laser (QCL) technology offer the potential for high-sensitivity and selective measurements of concentration and temperature for species of interest in combustion and propulsion applications. Here a mid-IR QCL sensor for carbon monoxide and temperature measurements operating at up to kHz detection bandwidths is demonstrated under scanned-wavelength direct-absorption and wavelength-modulation absorption spectroscopy operation. The sensor is capable of probing several CO transitions in the fundamental ro-vibrational band at frequencies from 2176 to 2189 cm^{-1} (wavelength of ~4.59 μm) where H_2O and CO_2 spectral interference is minimal. Temperature measurements are made via two-line ratio techniques. The sensor has been shown, in direct absorption mode for a one kHz detection bandwidth and at one atmosphere of total pressure, to provide sensitive temperature measurements from 950 to 3500 K and CO detection limits down to ~400 ppb per meter of absorption path length at room temperature and ~10 ppm per meter of absorption path length at 3500 K. In wavelength-modulation mode the sensor has been shown to provide thermometry from 850 to 3500 K and CO detection limits approximately one order-of-magnitude lower than those exhibited in direct-absorption operation (room temperature atmospheric pressure CO detection limit of ~30 ppb per meter of absorption path length). Demonstrations made in atmospheric pressure premixed ethylene/oxygen flames (Φ = 0.7-1.4) supported on a McKenna flat-flame burner are in excellent agreement at stoichiometric to rich conditions with thermocouple measurements and chemical equilibrium CO concentrations. At lean conditions sensor temperature and CO determinations are lower and higher, respectively, than those measured via thermocouple or predicted using chemical equilibrium due to the cool-flame-edge effect and resulting in incomplete reaction of CO to CO_2 at the flame edge. For sensor operation in direct-absorption mode in high-temperature shock tube experiments, measured CO mole fraction and temperature agree with post-reflected-shock conditions within ±1.5% and ±1.2% (1σ deviation), respectively. Under wavelength-modulation operation, sensor temperature measurements agree within ±1.9% (1σ deviation) with post-reflected-shock temperatures, but again the sensor provides CO sensitivity approximately one order-of-magnitude greater than those observed under direct-absorption operation. To the PI's knowledge, the thermometry measurements presented here represent the first high-temperature thermometry measurements made using a QCL.

2. Introduction

Laser absorption spectroscopy has long been used for line-of-sight measurements of parameters of importance in combustion and propulsion engine environments [1-2] due to its non-intrusive, sensitive, and selective nature. These include measurements of species concentration, temperature, pressure, density, mass flux, and velocity, which have proven useful for studying governing physical-chemical phenomena, developing combustion and propulsion device designs, and evaluating and validating simulations.

While there have been previous mid-infrared (mid-IR) lead-salt diode laser absorption measurements made in high-temperature combustion environments dating back to the late 1970s [3-4], much of the work related to laser absorption for combustion measurements has in the last twenty years been aimed at developing sensors that utilize overtone ro-vibrational transitions in the near-IR, largely due to the rapid maturation of telecommunications lasers [2] in the near-IR and the lack of robust mid-IR laser sources. Mid-IR lead-salt diode lasers are multi-mode, low-power (μW), and require cryogenic cooling. However, the overtone bands in the near-IR have significantly weaker absorption strengths than the fundamental ro-vibrational bands in the mid-IR. In the case of carbon monoxide, the absorption strength declines approximately two orders of magnitude for each overtone order (see Figure 1).

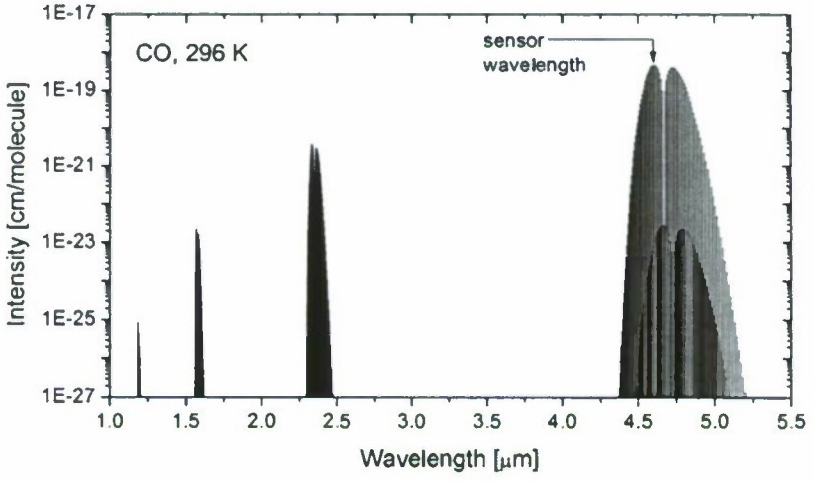

Figure 1. Carbon monoxide transition intensities at 296 K in the infrared (source: HITRAN 2004 [5]).

Mid-IR quantum cascade lasers (QCLs) have improved substantially in terms of their optical, electrical, and thermal characteristics since they were first demonstrated in 1994 [6]. Currently commercially available DFB-QCLs are capable of operating in pulsed or continuous wave (cw) mode at room temperature (thermoelectric cooling), providing the high-power (mW), narrow line width, single-frequency, and tunable mid-IR laser radiation required for sensitive detection of gas-phase species [7-8].

As QCLs have matured, several groups have developed absorption sensors based on these mid-IR sources, primarily for trace gas detection in environmental or biological applications, including: atmospheric [9] and volcanic monitoring [10], human breath analysis [11-12], and cigarette smoke analysis [13]. Mid-IR QCL based laser absorption sensors have also found limited use in high-temperature combustion environments. Previous work towards the application of mid-IR QCL absorption sensors to combustion and other high-temperature environments include the measurements of Wehe et al. [14-15] for NO and CO, at 5.26 and 4.62 μm respectively, in flame exhaust gases at moderate temperatures (~600 and ~1150 K). Wysocki et al. [16] measured NO up to 630 K in a gas cell using a pulsed QCL at 1900 cm^{-1} to demonstrate the potential of QCL absorption sub-ppm NO sensing in industrial exhaust gases. Recently, Chao et al. [17] demonstrated NO sensing near 5.2 μm using a broadly tunable (1890-1950 cm^{-1}) external-cavity QCL in a high-temperature gas cell (633 K), a laboratory exhaust rig (600 K, 20-95 ppm NO, 1.79 m path length), and the exhaust of a coal-fired power plant (~624 K, 80-120 ppm NO, 3 m path length).

Carbon monoxide, a harmful pollutant emission from combustion devices and an important indicator of combustion efficiency, is an ideal candidate for detection in the mid-IR because it is often found at low concentrations in exhaust gases. Detection of carbon monoxide in the mid-IR around 4.6 μm allows high-sensitivity measurements, not possible with near-IR CO sensors, and the potential for measurements with significantly shorter absorption path lengths. Additionally, the transitions in the CO fundamental band are extremely well characterized in terms of spectroscopic parameters (line position, line strength, and line broadening parameters), which allows direct interpretation of measurements through comparison with spectral simulation based on the wide array of accurate spectroscopic data available in the literature and makes CO a good starting point in the development of mid-IR QCL sensors for combustion gases.

In this project, a mid-IR QCL absorption sensor for CO and temperature, operating near 4.6 μm, was developed. The sensor can be operated in either scanned-wavelength direct-absorption mode or wavelength modulation spectroscopy (WMS) mode, for increased sensitivity, and provides both measurements of CO partial pressure (mole fraction for known pressure conditions) and temperature, using a two-line ratio technique. The sensor has been demonstrated in a room-temperature gas cell and high-temperature shock tube and flame environments. Under scanned-wavelength operation, the sensor is shown to provide accurate (±1-2%, for sufficient absorption) rapid (1-2 kHz bandwidth) thermometry for temperatures ranging from 950 to 3500 K and sensitivity to CO of 400 ppb/m path length at room temperature and 10 ppm/m path length at 3500 K. Under WMS operation, the sensor

was shown to provide accurate (±2%) thermometry from 850 to 3500 K at a detection bandwidth of 1 kHz, but with sensitivity to CO approximately one order-of-magnitude greater than that achieved using direct absorption (e.g., 30 ppb/m path length at room temperature).

The present thermometry measurements, while following a body of work in which a variety of mid-IR [4], near-IR [18-21], and ultraviolet [22-23] sources have been applied for shock tube and flame thermometry, represent the first demonstration of a QCL absorption sensor for thermometry in combustion or combustion-like environments, to the PI's knowledge, and span a very large temperature range (850-3500 K) of interest in combustion and propulsion applications.

3. Theory and Line Selection

3.1 Direct Absorption

The basic theory of direct absorption spectroscopy has been described numerous times; for example, see [24]. The absorption of monochromatic radiation along a line-of-sight is governed by the Beer-Lambert relation

$$\left.\frac{I}{I_0}\right|_\nu = e^{-\alpha_\nu L}$$

where I and I_0 are the transmitted and incident intensities, L the optical path length, ν the frequency of radiation, $\alpha_\nu L$ the absorbance, and α_ν the spectral absorption coefficient defined as

$$\alpha_\nu = S(T)\varphi_\nu P_i$$

$S(T)$ is the temperature-dependent line strength for the probed transition, P_i the partial pressure of the absorbing species, and φ_ν the line shape function, which is often approximated with a Voigt function for collisional and Doppler broadened transitions. The line strength for a transition can be written in terms of molecular and transition specific parameters and temperature as follows:

$$S(T) = S(T_0)\frac{Q(T_0)}{Q(T)}\left(\frac{T_0}{T}\right) exp\left[-\frac{hcE''}{k_B}\left(\frac{1}{T}-\frac{1}{T_0}\right)\right] \times \left[1-exp\left(\frac{-hc\nu_0}{k_B T}\right)\right]\left[1-exp\left(\frac{-hc\nu_0}{k_B T_0}\right)\right]^{-1}$$

where $Q(T)$ is the partition function, E'' the lower-state energy for the transition, ν_0 the line-center frequency, T_0 a reference temperature where the line strength is known (296 K in this work), h Planck's constant, c the speed of light, and k_B Boltzmann's constant.

Transitions with sufficiently different lower-state energies E'' can be used for determination of temperature due to the variation in line strength temperature dependence with lower-state energies:

$$S_1(T)/S_2(T) = f(T)$$

Two-line absorbance ratio temperature determinations can be made through measurement of the ratio of the integrated area for two transitions, a direct measurement of the ratio of line strengths, or by

measurement of the ratio of peak line-center absorbance for two transitions, which reduces to the ratio of line strengths for transitions with the same line shape function φ_v but more generally must be interpreted via spectral simulations at known pressure.

For the development of the sensor described here, CO transition near the peak of both the P and R branches of the CO fundamental ro-vibrational band near 4.6 μm were considered. Spectral simulations were performed using the HITRAN 2004 database for a number of potential CO line pairs at a broad range of conditions of relevance to combustion environments (296-3500 K, 0.1-50 atm, and variations in mixture). Line pairs were chosen based on absorption strength, isolation from interfering absorption (CO, CO_2, and H_2O absorption was considered), temperature sensitivity, and the availability of QCL sources in the frequency region of interest. Additionally, preference was given to line pairs that could be scanned with a single laser.

Two sets of neighboring line pairs were chosen, the R(9) and R(17) line pair near 2179 cm^{-1} and the R(10) and R(18) line pair near 2183 cm^{-1}; see Tables 1 and 2 for spectroscopic parameters for these four transitions. A spectral simulation for the frequency region of the chosen CO lines for atmospheric pressure combustion-like conditions (2000 K, 1 atm, 0.1% CO, 10% H_2O, and an absorption path length of 10 cm) is shown in Figure 2 and a simulation for an elevated pressure condition (10 atm) is shown in Figure 3; Figures 2 and 3 also show the frequency scanning range of the sensor (~12 cm^{-1}). Figure 2 illustrates that the chosen transitions are sufficiently isolated from interfering absorption from H_2O at atmospheric pressure and 2000 K, for a ratio in H_2O to CO concentration of 100; interference from CO_2 was found to be negligible at all conditions in the frequency range of interest. However, at higher pressures the R(9) suffers slight interference from a neighboring H_2O transition at temperatures of 2000 K and higher, as illustrated in Figure 3. It should be pointed out that at lower temperatures (300-1500 K) the H_2O interfering absorption is much weaker and the CO transitions are isolated for much greater ratios in H_2O to CO concentration, particularly at pressures below 5 atm.

Table 1. Spectroscopic parameters for CO transitions.

Transition	Line-center frequency, v_0 [cm^{-1}]	Lower-state energy, E'' [cm^{-1}]	Line strength, S (296 K) [$cm^{-2}atm^{-1}$]	
			HITRAN 2004 [5]	Measured
R(9), low-T	2179.7719	172.98	10.11 ± 0.20	10.24 ± 0.41
R(10), low-T	2183.2238	211.40	9.24 ± 0.18	9.16 ± 0.37
R(17), high-T	2179.2438	2725.63	1.48 (±0.03) × 10^{-4}	
R(18), high-T	2182.3636	2794.07	1.13 (±0.02) × 10^{-4}	

Table 2. Collisional broadening parameters for CO transitions.

Transition	Line-center frequency, v_0 [cm^{-1}]	Collisional broadening parameters of the form $\gamma_i(T) = \gamma_i(T_0)\left(\frac{T_0}{T}\right)^{n_i}$, where T_0 = 296 K.							
		CO-air [5]		CO-CO [5]		CO-Ar [25]		CO-He [26]	
		$\gamma_{N_2}(T_0)$	n_{N_2}	$\gamma_{CO}(T_0)$	n_{CO}	$\gamma_{Ar}(T_0)$	n_{Ar}	$\gamma_{He}(T_0)$	n_{He}
R(9)	2179.7719	0.0580	0.750	0.0643	-0.00255	0.0465	0.720	0.0468	0.583
R(10)	2183.2238	0.0573	0.750	0.0632	-0.00254	0.0459	0.710	0.0470	0.583
R(17)	2179.2438	0.0527	0.680	0.0572	0	0.0423	0.699	0.0466	0.556
R(18)	2182.3636	0.0519	0.670	0.0563	0	0.0417	0.699	0.0465	0.552

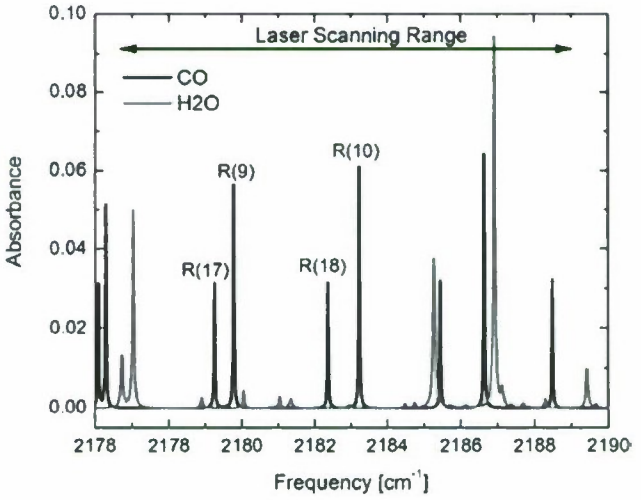

Figure 2. Simulated spectra in the frequency region of the developed CO sensor for 0.1% CO and 10% H_2O in air at 2000 K, 1 atm, and a pathlength of 10 cm (performed using HITRAN 2004 database [5] with air as exclusive collision partner).

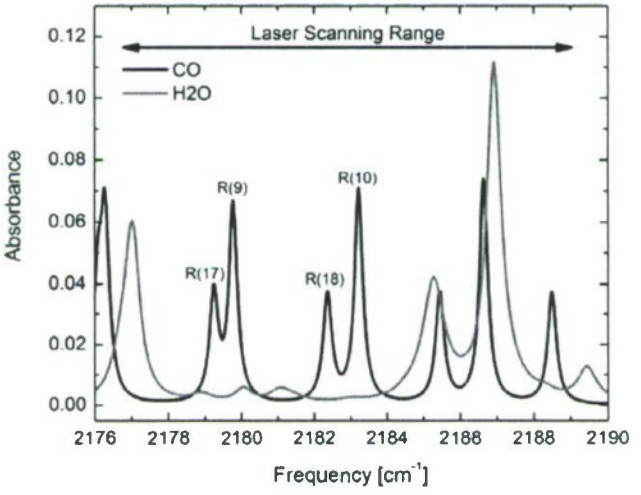

Figure 3. Simulated spectra in the frequency region of the developed CO sensor for 0.1% CO and 10% H_2O in air at 2000 K, 10 atm, and a pathlength of 10 cm (performed using HITRAN 2004 database [5] with air as exclusive collision partner).

The transitions in the CO fundamental band, including those selected here, have been the subject of numerous experimental spectroscopic studies which have accurately quantified the line positions [27-29], line strengths [29-33], and collision broadening [25-26,33-38] and shift parameters [16,33,36]. The spectroscopic parameters (line centers, lower state energies, line strengths, and collisional broadening parameters) used here are given in Tables 1 and 2. Due to the relatively low-pressure conditions encountered in the experiments performed, collisional line shifts were not considered in simulations. For spectral simulations and in Table 2, collisional broadening was defined using the formulation

$$\gamma_i(T) = \gamma_i(T_0)\left(\frac{T_0}{T}\right)^{n_i}$$

where $\gamma_i(T)$ is the collisional broadening coefficient at temperature T for collisions of the i^{th} bath gas with the absorbing species (CO here), $\gamma_i(T_0)$ is the collisional broadening coefficient at the reference temperature T_0 = 296 K, and n_i is the collisional broadening temperature exponent for collisions involving the i^{th} bath gas with the absorbing species. The collisional broadening half width (FWHM), $\Delta\nu_C$, is given by

$$\Delta\nu_C = P\sum_i X_i 2\gamma_i$$

where P is the total pressure and X_i the mole fraction of the i^{th} bath gas collision partner. The spectroscopic parameters given in Tables 1 and 2 and used in all simulations presented were taken mostly from HITRAN 2004 [5] with collisional broadening parameters for CO-Ar and CO-He mixtures taken from recent measurements of Thibault et al. [25] and Mantz et al. [26], respectively.

For thermometry in high-temperature gases containing CO, line strength ratios for both the R(9) and R(17) and R(10) and R(18) line pairs provide sufficient sensitivity at a large range of temperatures; both of these line pairs have differences in lower-state energies of greater than 2500 cm^{-1} (see Table 1). In Figure 4 both the line strength ratio, $R(T) = S_1(T)/S_2(T)$, and the sensitivity of the ratio to temperature, $(dR/R)/(dT/T)$, are plotted for both line pairs from 500 to 3000 K. Generally the sensitivity should be larger than unity for low-uncertainty temperature measurements; this is the case for all temperatures shown in Figure 4 and temperatures up to ~4000 K. However, temperature measurements are limited to temperatures in excess of ~900 K due to insufficient absorption strength for the high-temperature R(17) and R(18) lines at lower temperatures. Both pairs of transitions provide similar temperature dependence and sensitivity. Hence, the selection of the optimal transition pair for a particular measurement is based on desired scan rate and pressure. At slightly elevated pressures the R(10) and R(18), which are more separated (0.86 cm^{-1}), provide less line blending and H_2O interference.

At pressures near atmospheric and high temperatures, conditions for which collisional broadening is minimized, the R(9) and R(17) transitions can be scanned somewhat more rapidly using less variation in laser injection current due their smaller separation in frequency (0.53 cm^{-1}).

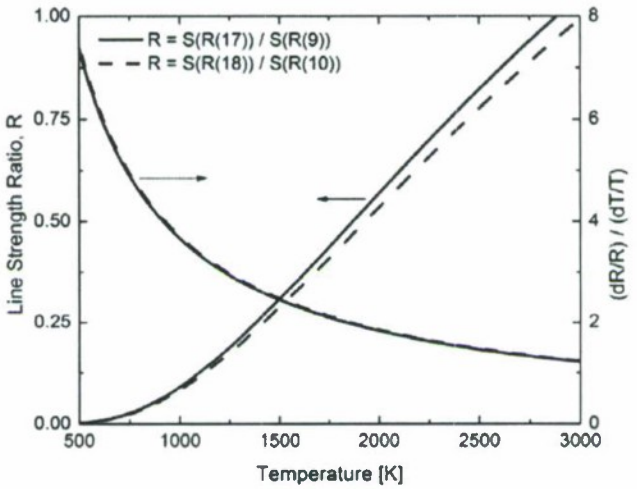

Figure 4. Line strength ratios and ratio temperature sensitivities for the R(17) and R(9) and R(18) and R(10) line pairs.

3.2 Wavelength Modulation Spectroscopy

The fundamental theory of wavelength modulation spectroscopy (WMS) with harmonic detection has been available in the literature, at various levels of rigor, for more than 40 years [39-40]. Here we follow the derivations laid out by Reid and Labrie [41], Philippe and Hanson [18], and Li et al. [42], who also followed the general theory of Kluczynski and Axner [43], which are suitable for applications where the laser intensity is dependent on frequency. The increased sensitivity of WMS techniques relative to direct absorption can be attributed to a shift in detection to higher frequencies, relative to the half width of the absorbing transition, to reduce $1/f$ noise. Higher frequencies are attained by superimposing a sinusoidal wave onto the laser injection current resulting in a frequency and intensity modulation of the form:

$$\nu(t) = \bar{\nu} + a \cdot \cos(\omega_m t)$$

$$I_0(t) = \bar{I_0}[1 + i_0 \cdot \cos(\omega_m t + \psi_1)]$$

where ω_m is the modulation angular frequency, a the modulation depth, i_0 the linear laser intensity modulation, ψ_1 the phase shift between intensity and frequency modulation, and $\bar{\nu}$ and $\bar{I_0}$ the average laser frequency and intensity (here the local average during the slow laser frequency scan). Depending on the response of the laser to injection current modulation at the modulation depth, a, of interest, additional terms may be required:

$$I_0(t) = \bar{I_0}[1 + i_0 \cdot \cos(\omega_m t + \psi_1) + i_2 \cdot \cos(2\omega_m t + \psi_2)]$$

where i_2 and ψ_2 account for nonlinear intensity-frequency modulation; additional higher-order harmonic terms can be added should they be required to adequately characterize the intensity-frequency modulation of a specific laser. For the QCL utilized here at modest modulation depths the nonlinear intensity term, i_2, was measured to be relatively small at the modulation conditions of interest, $i_2 / i_0 =$ 0.004, and was neglected for simplicity (see next section).

The transmitted intensity, $I(t)$, is related to the incident intensity, $I_0(t)$, via Beer's law:

$$I(t) = I_0(t) \cdot \exp\big(-\alpha\big(\nu(t)\big)L\big) = I_0(t) \cdot \tau(\nu(t))$$

where $\tau(\nu(t))$ is the transmission coefficient, $\alpha(\nu(t))$ the absorption coefficient, and L the path length for absorption. The transmission coefficient, an even periodic function in time, can be expanded in a Fourier cosine series:

$$\tau(\bar{\nu} + a \cdot \cos(\omega_m t)) = \sum_{k=0}^{\infty} H_k(\bar{\nu}, a) \cdot \cos\,(k\omega_m t)$$

where $H_k(\bar{\nu}, a)$, the kth harmonic Fourier component, is given by:

$$H_0(\bar{\nu}, a) = \frac{1}{2\pi}\int_{-\pi}^{\pi} \tau(\bar{\nu} + a \cdot \cos\theta)d\theta$$

$$H_k(\bar{\nu}, a) = \frac{1}{\pi}\int_{-\pi}^{\pi} \tau(\bar{\nu} + a \cdot \cos\theta)\cos k\theta\, d\theta$$

For optically thin conditions (i.e., $\alpha(\nu)L \ll 1$), the transmission coefficient can be simplified:

$$\tau = \exp(-\alpha L) \approx 1 - \alpha L = 1 - S\varphi P_i L$$

where S is the line strength, φ the line shape, and P_i the partial pressure of the absorbing species. Upon combination of H_k with τ, the kth harmonic Fourier coefficient reduces to:

$$H_k(\bar{\nu}, a) = -\frac{SP_iL}{\pi}\int_{-\pi}^{\pi} \varphi(\bar{\nu} + a \cdot \cos\theta)\cos k\theta\, d\theta$$

In practice a lock-in amplifier is used to isolate the harmonic chosen for detection. The lowest harmonics provide the strongest signals. The even harmonics are of interest due to their symmetry, providing peak signals at line center, resulting in easy interpretation. As such, the second harmonic is often utilized in WMS, as is the case here. The isolated second-harmonic signal (WMS-2f) is given by:

$$S_2(\bar{\nu}) = G\bar{I_0}\left[\frac{i_0}{2}H_3(\bar{\nu}, a)\cos(2\psi + \Omega) + H_2(\bar{\nu}, a)\cos(\psi + \Omega) + \frac{i_0}{2}H_1(\bar{\nu}, a)\cos\Omega\right]$$

where Ω is the phase shift between laser emission intensity and detection signal and here is adjusted, within automated acquisition software, to maximize the WMS-2f signal and G is the optical-electrical gain in the detection system.

The first-harmonic signal (WMS-1*f*) can also be extracted using lock-in amplification and is given by:

$$S_1(\bar{\nu}) = G\overline{I_0}\left[\frac{i_0}{2}H_2(\bar{\nu},a)\cos(2\psi+\Omega) + H_1(\bar{\nu},a)\cos(\psi+\Omega) + i_0 H_0(\bar{\nu},a)\cos\Omega\right]$$

The WMS-1*f* signal can be used to normalize the WMS-2*f* signal to cancel out the gain *G* and the average laser intensity $\overline{I_0}$. Here, measured WMS-2*f* peak heights are normalized by the WMS-1*f* peak heights for quantitative detection of the absorber:

$$S_{2f/1f} = S_{2,max}/S_{1,max}$$

It should be pointed out that this analysis neglects nonlinear intensity-frequency modulation, which results in residual-amplitude modulation (RAM) [42], and relies on adjustment of phase shift between detection and laser intensity Ω to zero to eliminate the need to capture both the x- and y-components of the harmonic signals, as described by Li et al. [42] and references therein. These two simplifications are suitable for the relatively small modulation depths utilized here, where non-linear intensity-frequency modulation is insignificant, and because the phase shift Ω is adjusted to zero through automated software adjustment to maximize WMS-2*f* signals.

Similarly to direct absorption, WMS can be used to determine gas temperature by considering the ratio of 1*f* normalized WMS-2*f* peak heights for two transitions with sufficiently different lower-state energies and within a sensitive temperature range:

$$R(T) = \frac{S_{2f/1f}\big|_{\nu_1}}{S_{2f/1f}\big|_{\nu_2}}$$

4. Sensor Architecture and Operation

The QCL used here for CO and thermometry sensing was procured from Alpes Lasers (Alpes model # sbcw1960). The QCL was mounted in a sealed laser housing (Alpes LLH-100) and cooled with a thermoelectric Peltier cooler and an Alpes TCU151 temperature controller. Current was sent to the laser through the combination of a ILX Lightwave LDX-3232 laser controller, coupled to a function generator (Agilent 33220A), which was supplied with arbitrary waveforms from National Instruments LabVIEW software to scan and if desired modulate the QCL. The QCL is capable of producing radiation at frequencies from 2176.8 to 2188.9 cm^{-1} which can be tuned through variation in injection current (limited to 600 mA or less) and base temperature (limited to -30 to 5 °C). The QCL can be rapidly scanned (we performed scan rates up to 10 kHz), through saw tooth modulation of the injection current, from 1 to 5 cm^{-1} in frequency, depending on base temperature, with peak optical powers of ~25 mW. In

this work typically 1-2 cm^{-1} of frequency tuning was used to probe one of more CO transitions. The laser line width was not measured but is expected to be less than 10 MHz based on previous line width studies for room-temperature cw-QCLs [44-45]; in this work the transition half widths, typically around 1.5 GHz, are significantly larger than the laser line width.

A schematic of the experimental setup used for scanned-wavelength direct-absorption measurements is given in Figure 5. The output of the QCL was collimated with a ZnSe aspheric lens (*f* / 0.9) from Janos and passed through the absorbing medium of interest, in this work either a gas cell, shock tube, or flat flame. Prior to transmittance, a portion of the beam was split using a ZnSe beam splitter and sent to a solid silicon etalon (FSR = 0.020 cm^{-1}) for relative frequency calibration. Absolute frequencies were determined from the known CO line center positions. Laser intensities were measured using LN_2 cooled InSb detectors from Infrared Associates (model IS 2.0, adjustable gains and bandwidth up to 5 MHz) and recorded using a computerized data acquisition system.

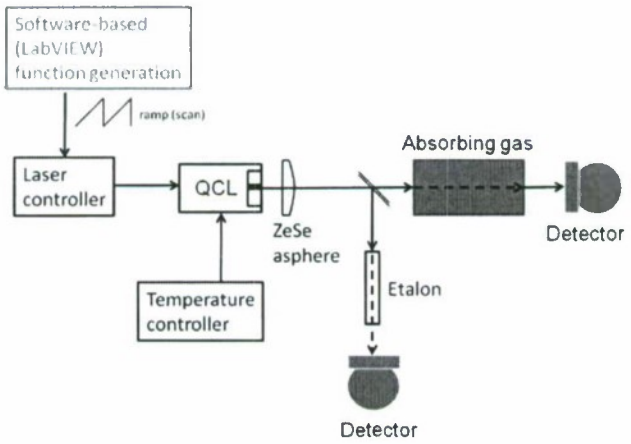

Figure 5. Experimental setup for scanned-wavelength direct-absorption measurements.

For WMS measurements, the combination of a low-frequency ramp (500 Hz and 1 kHz) and a high-frequency sinusoidal modulation (50 kHz) was supplied to the QCL as injection current and the first and second harmonic signals were extracted using a software lock-in amplifier (low-pass filter at 15 kHz) coded within a LabVIEW data acquisition program. See Figure 6 for a schematic of the experimental components and the data acquisition and analysis for WMS operation. QCL frequency/intensity modulation and all signal reduction, as described in this and the preceding section, was implemented using LabVIEW software.

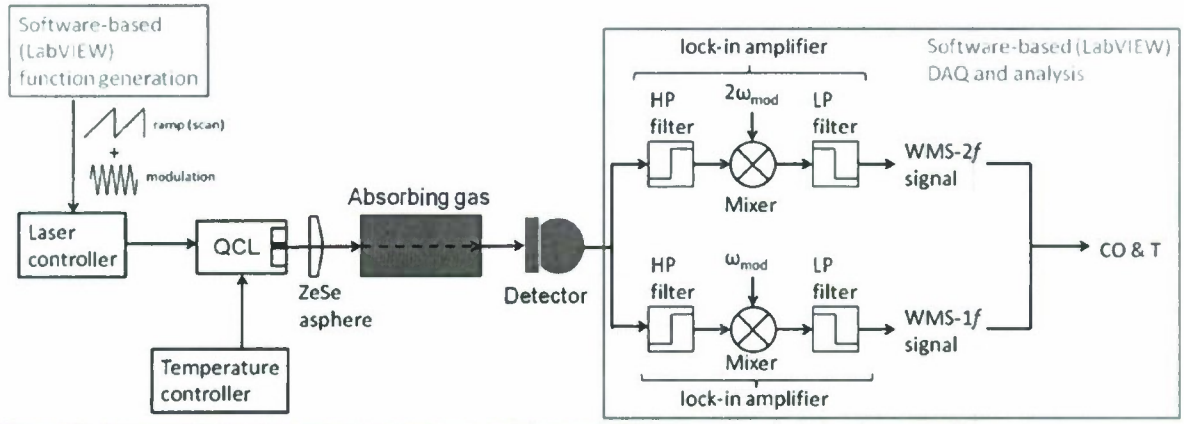

Figure 6. Schematic of WMS sensor hardware and data acquisition and analysis implementation.

To determine the optimal modulating parameters for the sensor in WMS operation, simulations of the WMS second harmonic (WMS-2*f*) line shapes were performed, using the spectroscopic parameters given in Tables 1 and 2 and accounting for both Doppler and collisional line broadening, for a range of operating modulation depths, a, for the CO transitions of interest at a range of temperatures at a pressure of 1 atm. The results for the peak WMS-2*f* heights for the R(9) and R(17) lines, normalized to unity for a range of modulation depths, are displayed in Figure 7 for a 0.1%CO/air mixture at 1 atm and temperature ranging from 1000 to 3000 K. As the figure illustrates, the optimum modulation depth, providing maximum WMS-2*f* peak height, increases with decreasing temperature due to the increase in line width with decreasing temperature. The maximum WMS-2*f* peak height is known to occur for a modulation index (defined as $m = \Delta v/a$, where m is the modulation index and Δv is the transition half width) around 2.2 [42]. Because it is not practical to adjust the operating modulation depth on the fly when probing gases of unknown temperature, a single operating modulation depth was chosen such that WMS-2*f* signals were optimized for a range of temperatures. For the high-temperature thermometry measurements made here, a modulation depth of 0.04 cm^{-1} was chosen. As shown in Figure 7, a = 0.04 cm^{-1} provides WMS-2*f* peak heights which are at most reduced by 4% from their maximum at the extremes in temperature shown, 1000 and 3000 K. Additionally, the normalized WMS-2*f* peak heights for the low- and high-temperature transitions, R(9) and R(17) respectively, in Figure 4 are nearly functionally identical. This indicates that two-line WMS-2*f* measurements with a single modulation depth can be optimized for both lines. Also, any degree of off-optimum operation affects both lines nearly the same and will cancel out in the two-line-ratio temperature determinations. This is illustrated in Figure 8 where the variation in the simulated WMS-2*f* peak height ratio for the R(9) and R(17) lines for a large range of modulation depths is shown. The figure demonstrates that the WMS-2*f* peak height ratio shows little sensitivity to modulation depth and that the optimized modulation depth,

a = 0.04 cm^{-1}, nearly coincides with the direct absorption line strength ratio. The results shown in both Figures 7 and 8 for the R(9) and R(17) line pair are similar for the R(10) and R(18) line pair and all the conclusions hold.

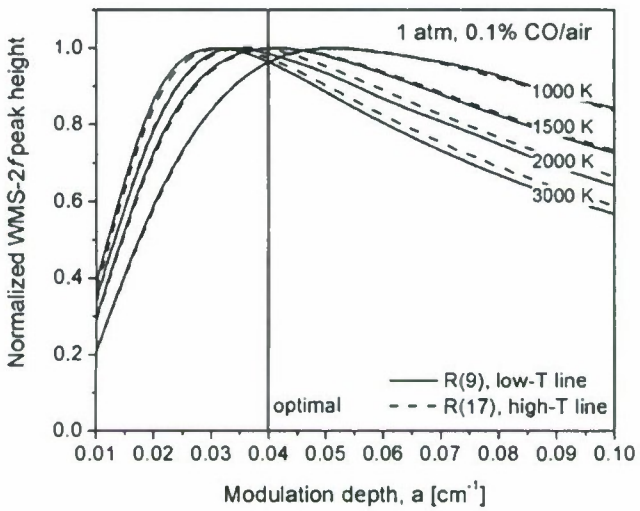

Figure 7. Simulated variation of WMS-2f peak height (normalized such that the maximum is unity) with modulation depth for the R(9) and R(17) lines and for a 0.1% CO/air mixture at 1 atm and 1000, 1500, 2000, and 3000 K.

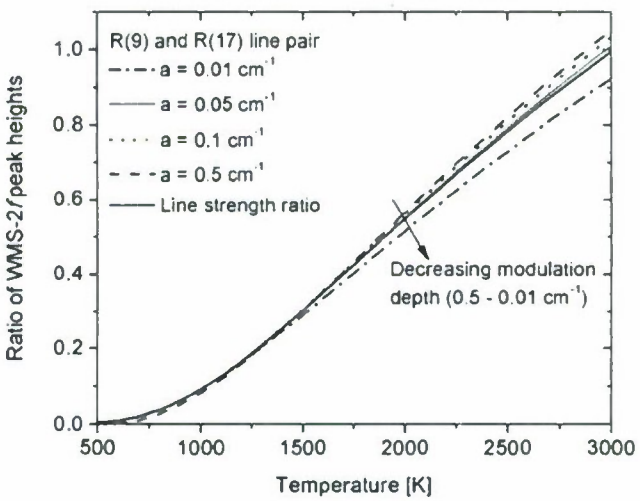

Figure 8. The simulated variation of the ratio of WMS-2f peak heights for the R(9) and R(17) lines with temperature for a range of modulation depths. The ratio of line strengths for these two transitions is also given.

Prior to implementation of the QCL-based sensor for WMS measurements, the QCL response to current modulation, as described in the earlier section (i.e., $\nu(t) = \bar{\nu} + a \cdot \cos(\omega_m t)$ and $I_0(t) = \overline{I_0}[1 + i_0 \cdot \cos(\omega_m t + \psi_1)]$), was characterized. To do so, the QCL injection current was modulated and

the mid-IR output was split. One portion was sent directly to an LN_2-cooled InSb detector and the other through a solid silicon etalon (FSR = 0.020 cm^{-1}) prior to detection on a second LN_2-cooled InSb detector. This allowed measurement of frequency and intensity as a function of time which in turn provided direct determination of the dependence of modulation depth a on injection current i_0, the intensity/frequency modulation phase shift Ψ_1, and the residual non-linear intensity term, i_2, as a function of modulation depth. For the chosen optimum modulation depth, a = 0.04 cm^{-1}, and for a chosen modulation frequency of f = 50 kHz, the following represents the laser intensity:

$$I_0(t) = \bar{I_0}[1 + 0.138(\pm 0.001) \cdot \cos(2\pi(50 \times 10^3 s^{-1})t + 1.11(\pm 0.03)\pi)]$$

A modulation frequency of 50 kHz was chosen for this work to provide sufficient separation between the frequencies for modulation (50 kHz), lock-in amplification (15 kHz low-pass filter), and laser frequency scanning (500 Hz and 1 kHz). The non-linear intensity modulation term, i_2, given in the earlier section (i.e., $I_0(t) = \bar{I_0}[1 + i_0 \cdot \cos(\omega_m t + \psi_1) + i_2 \cdot \cos(2\omega_m t + \psi_2)]$) was also characterized. For a = 0.04 cm^{-1} and f = 50 kHz, i_2 was found to be small relative to i_0 (i_2/i_0 = 0.004) and was neglected in this work for simplicity. It should be pointed out that because we are probing CO transitions at near atmospheric pressure and high temperatures, the transition half widths are quite small (~0.06-0.1 cm^{-1}) and therefore both a and i_0 are small and also the non-linear i_2 term is small. This is simply because we are not modulating the laser very hard, relative to in other studies (e.g., [42]), which results in little non-linear modulation. If we were to probe CO at higher pressures both a and i_0 would be larger and the i_2 term likely important.

S. Scanned-Wavelength Direct-Absorption Sensor Demonstrations

S.1 Low-Temperature Gas Cell Measurements

Prior to application of the sensor to high-temperature gases, the sensor was initially tested in measurements of the room-temperature line strengths for the R(9) and R(10) transitions in a gas cell for comparison to the well documented values found in the HITRAN 2004 database which have uncertainty of at most ±2% based on a survey of the literature [5,29-33]. Additionally, quantitative line shape measurements for the R(9) and R(10) transitions were made at room temperature (297 K) at pressures from 200 to 800 Torr for comparison to HITRAN-based simulations. All measurements proved to be in good agreement with spectral simulations.

Example experimental transmitted and reference intensity traces are shown in Figure 9 for a scan of the R(10) line for a gas mixture containing 0.116%-molar CO in N_2 at a total pressure of 353.6 Torr at 297 K. In this example the QCL temperature was set to -15 °C and the current supplied to the QCL

was ramped using a saw tooth function from 350 mA to 550 mA at 1 kHz. As illustrated in Figure 9, at 0.15 ms the QCL reaches the threshold current for lasing and from that time forward the intensity rises approximately linearly until 1.0 ms when the current supplied returns to 350 mA, below the lasing threshold. For the determination of absorbance via the Beer-Lambert relation, baseline reference intensities were both measured in the evacuated gas cell, as in Figure 9, and inferred by subtracting the absorbing feature from the transmitted intensity and fitting a polynomial.

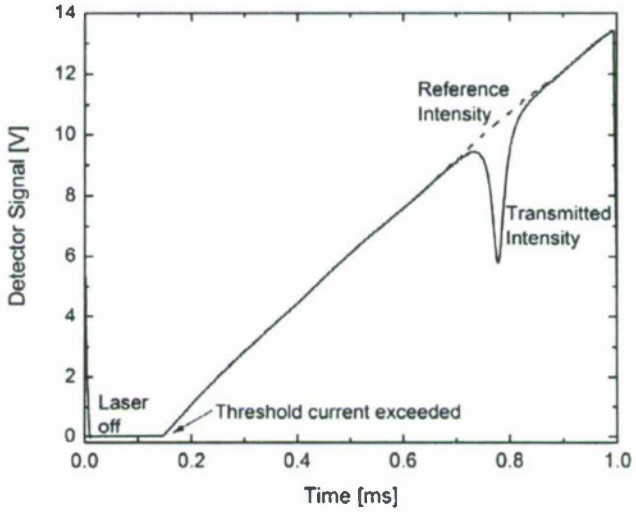

Figure 9. Example raw traces for transmitted and reference intensity for a frequency-scan of the R(10) line. Conditions: 0.116% CO/N_2, 353.6 Torr, and 297 K.

The measured absorbance, determined using the Beer-Lambert relation and the etalon trace for relative frequency, for the raw intensity traces shown in Figure 9 is shown in Figure 10. The measurement is compared to a spectral simulation performed using the HITRAN 2004 database with good agreement. Measurements such as that illustrated in Figure 10 were made for a large number of CO/N_2 and CO/Ar mixtures at conditions ranging from 200-800 Torr at 297 K with good agreement for all measurements with simulations based on the HITRAN 2004 database and supplemental broadening parameters for CO-Ar mixtures given in Table 2 (previous section).

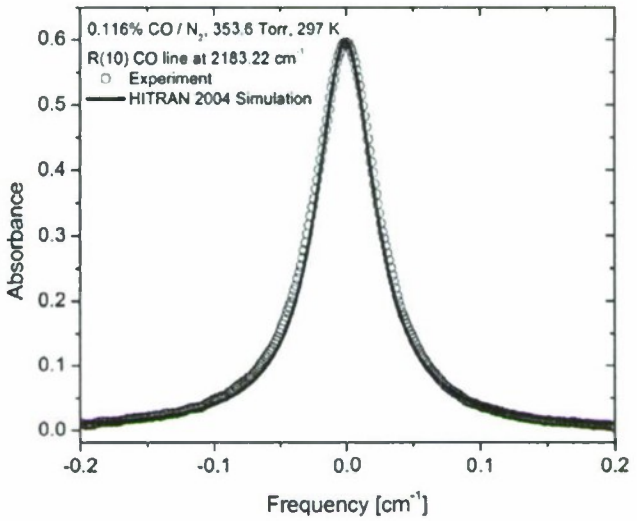

Figure 10. Absorption trace for the frequency scan of the R(10) line shown in Figure 9 with comparison to spectral simulation performed using HITRAN 2004 [5].

For the measurement of room-temperature line strengths for the R(9) and R(10) transitions, quantitative measurements of line shape were fit with Voigt profiles and the integrated areas under the Voigt fits were determined. A representative measurement of absorbance for the R(9) line is shown in Figure 11 with a Voigt fit and peak-normalized residual values for the fit.

For determination of line strengths, measurements were made for a variety of dilute CO/N_2 mixtures at total pressures around 350 Torr and 760 Torr at 297 K. Dilute CO/N_2 mixtures were required to attain appropriate peak absorbance values for the strong transitions probed and the mixture total pressures were chosen such that mixtures provided low uncertainty in CO partial pressure. A linear fit to the variation of measured integrated area per unit path length with CO partial pressure allows determination of line strengths for the R(9) and R(10) transitions, see Figure 12. The measured line strengths are in good agreement with the values found in the HITRAN 2004 database (see Table 1, previous section). The measured line strengths given in Figure 12 differ slightly with those given in Table 1 due to the conversion from the 297 K measurement temperature to 296 K, the temperature at which the HITRAN values are tabulated.

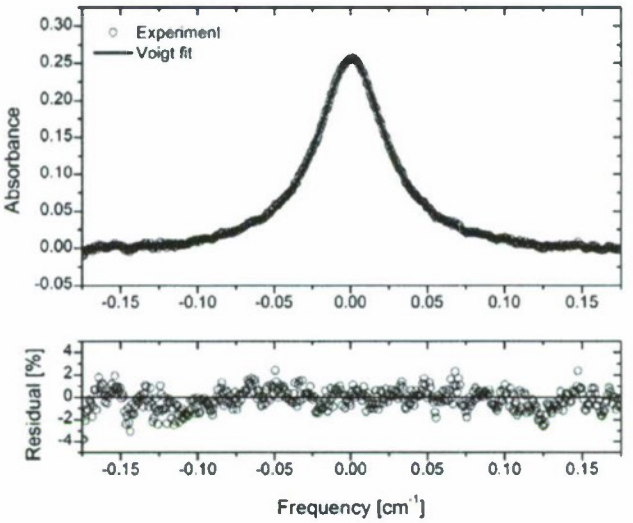

Figure 11. Example measured absorbance for the R(9) line with Voigt fit and residual (defined as % of peak absorbance). Conditions: 0.048% CO / N_2, 351.5 Torr, 297 K.

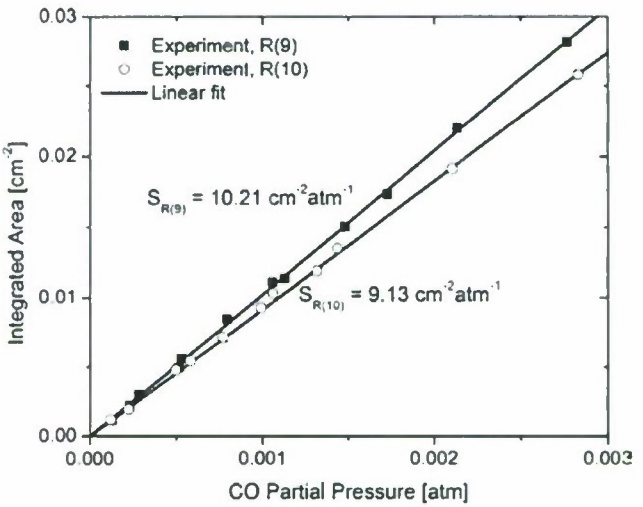

Figure 12. Measured integrated areas for the R(9) and R(10) lines as a function of CO partial pressure for determination of line strengths at 297 K.

It should be pointed out that the spectroscopic parameters in HITRAN for the mid-IR CO transitions probed here have small uncertainty, particularly relative to those for other molecules. Therefore, the line strength measurements, which have greater uncertainty than the line strengths values in HITRAN, are a validation of the sensor and analysis techniques rather than the HITRAN database. Likewise, the good agreement between quantitative spectral absorbance, as illustrated in the example in Figure 10, for the range of conditions studied in the gas cell provides validation of the sensor

at these conditions, as we have a high degree of confidence (approximately ±2% in absorbance across the line shape, based on uncertainties in line strength and broadening parameters) in the simulations of CO transitions based on HITRAN spectroscopic parameters.

Measurements were also carried out to quantify the sensor noise characteristics and minimum detectivity. In Figure 13 an absorbance measurement that results from a 1 kHz frequency scan of the R(9) CO transition for a room-temperature 430 Torr 17 ppm CO/Ar mixture with a path length of 10 cm is displayed. Figure 13 illustrates noise with a 1σ deviation of approximately ±0.002 in absorbance which corresponds to 2.4 ppm for the given experiment and 0.24 ppm per meter of path length at the given temperature (297 K) and pressure (430 Torr) and for a 1 kHz detection bandwidth. The noise limitation displayed in Figure 13 results primarily from a combination of high-frequency laser intensity noise and detector noise.

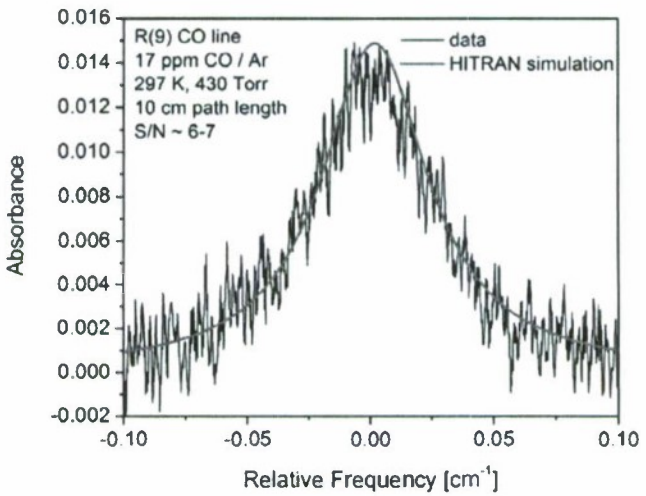

Figure 13. Demonstration of a noise floor of ±0.002 in absorbance for a 1 kHz scan of the R(9) CO line.

5.2 High-Temperature Shock Tube Measurements

For high-temperature validation and demonstration of the sensor under direct-absorption operation, scanned-wavelength CO measurements were performed in reflected shock experiments at pressures from 1 to 5 atm in a previously described shock tube [46]. Measurements were made using the hardware shown in Figure 5 with the QCL output transmitted through the shock tube (inner diameter of 12.3 cm) at a location 2 cm from the driven section end wall. Measurements were made in shock-heated gases (reflected shock region) for temperatures ranging from 950 to 3500 K and for mixtures containing various proportions of CO, argon, and helium. Helium was used to accelerate CO vibrational relaxation. Scanned-wavelength CO measurements were made in individual experiments for

either the R(9) and R(17) line pair and the R(10) and R(18) line pair at a scan rate (detection bandwidth) of 2 kHz. Figure 14 shows an example experiment for reflected shock conditions of 1673 K and 1.22 atm and a mixture of 0.270% CO/10% He/Ar. In this example the laser frequency is scanned over the R(9) and R(17) line pair.

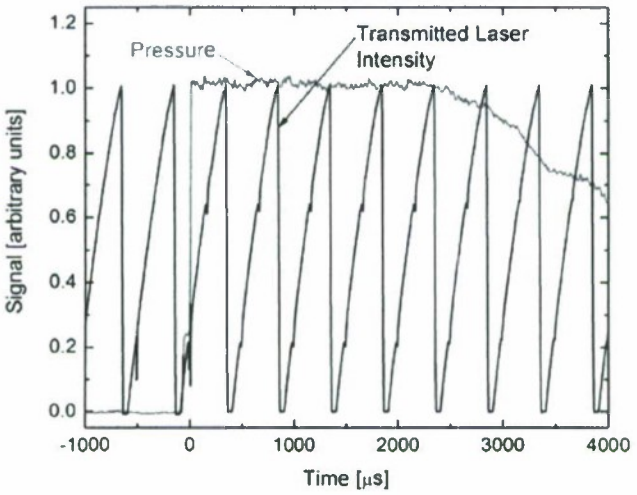

Figure 14. Example shock tube measurement (pressure and transmitted QCL intensity). Laser was scanned over both the R(9) and R(17) transitions at 2 kHz. Reflected shock conditions: 1673 K, 1.22 atm, 0.270% CO / 10% He / Ar.

For shock tube experiments, as shown in Figure 14, the baseline reference intensity was determined by examining a frequency scan prior to the passage of the incident shock. The low pressure conditions in the test gas prior to the incident shock made subtraction of the absorbing features and polynomial baseline fitting quite straight forward due to the extremely narrow low-pressure spectral features. Additionally, measurements of consecutive laser intensity scans showed negligible variation. The baseline and an extracted absorption scan from the reflected shock region were used to determine the absorbance via the Beer-Lambert relation, an example is shown in Figure 15.

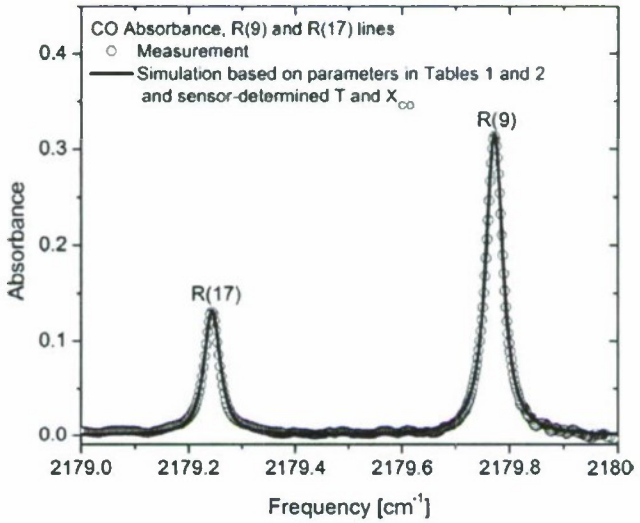

Figure 15. Example high-temperature (shock tube) CO absorbance measurement for the R(9) and R(17) transitions with comparison to simulation based on spectroscopic parameters in Table 1 and 2 and at sensor determined conditions. Reflected shock conditions: 1673 K, 1.22 atm, 0.270% CO / 10% He / Ar. Sensor measurements: 1684 K, 0.272% CO.

The temperature and CO mole fraction measurements reported here result from the first complete frequency scan following passage of the reflected shock. Although, typically the results of the first four frequency scans following the reflected shock yielded temperatures and CO mole fractions within 1.5% of each other. At longer shock tube test times the temperature decreases for low Mach number shocks due to gasdynamic interaction of the shock-heated gases with rarefaction waves emanating from the driver section, as shown in the Figure 14 example, or temperature increases for high Mach number shocks due to gasdynamic interaction of the reflected shock wave with the driven-gas-driver-gas contact surface. The relative laser scanning frequency was determined from a measured etalon trace and the absolute frequency was determined from the line-center frequencies of the R(9) and R(10) transitions.

For a measured absorbance trace, the temperature was determined by comparing the ratio in line-center peak absorbance with simulations performed using the HITRAN 2004 database and supplemental collisional broadening parameters given in Table 2 for variable temperatures and the known reflected shock pressure. The CO mole fraction was determined by comparison of the line-center peak absorbance of either the R(9) or R(10) lines with HITRAN simulations performed at the determined temperature and reflected shock pressure. A comparison of measured temperature versus reflected shock temperature is shown in Figure 16 and measured CO mole fraction normalized by mixture CO mole fraction is shown in Figure 17 for high-temperature shock tube experiments at pressures around

one atmosphere. The temperature and mole fraction measurements, which were made at 2 kHz measurement bandwidth, have 1σ deviations about the experimental values of 1.2% and 1.5%, respectively. The uncertainty in reflected shock temperature is approximately ±0.7% and the uncertainty in CO partial pressure is approximately ±1%. Hence, the measurements have deviations that are only slightly greater than the uncertainty in conditions and thus sensor measurement uncertainties are likely smaller than the reported deviations (±1.2 and ±1.5%).

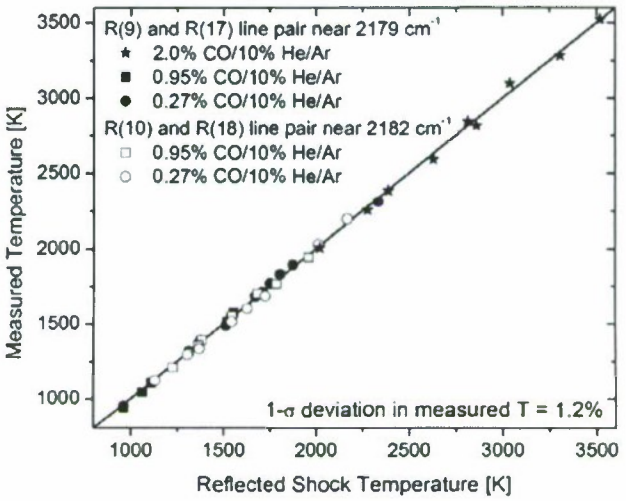

Figure 16. Temperature measurements for shock tube experiments performed around 1 atm.

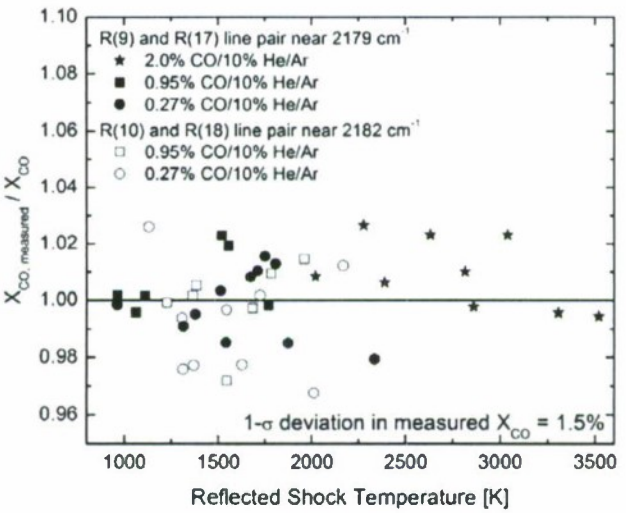

Figure 17. Measured CO mole fraction normalized by specified mixture CO mole fraction for shock tube experiments performed around 1 atm.

It was found that using peak absorbance and peak absorbance ratio for mole fraction and temperature determinations, for conditions with pressure known to within ±1%, provided better

agreement with the experimental values than mole fractions and temperatures determined using integrated absorbance and integrated absorbance ratio. This is due to the fact that the largest source of uncertainty in these measurements stems from error in the laser reference baseline intensity. The use of transition integrated areas for temperature and mole fraction results in a magnification of this uncertainty, through the integration of a constant source of error at all frequencies in the absorbance. However, for measurements at unknown pressure, integrated absorbance must be used for temperature and partial pressure (or concentration).

The positive results shown in Figures 16 and 17 for such a large range of temperatures illustrate the utility of this diagnostic for measurements requiring bandwidth of a few kHz or less. The strong mid-IR CO transitions probed by this sensor and the large differences in lower-state energies for the low- and high-temperature lines provide low-uncertainty measurements at a very large range of temperatures relevant to combustion. Although temperature measurements were only carried out for temperatures up to ~3500 K, sensitive thermometry using the this sensor and the two-line technique presented here is possible for temperatures up to 4000 K. At temperatures in excess of 4000 K the sensitivity of the two-line ratio technique begins to degrade somewhat (i.e., $(dR/R)/(dT/T)$ falls below unity). Due to the intensity of the transitions in the CO fundamental band, the sensor provides CO detection with orders-of-magnitude greater sensitivity than that provided by the overtone bands readily accessible by telecommunications lasers. Figure 18 illustrates the CO detection limits for 1 kHz bandwidth measurements at 1 atm for a range of temperature using a minimum detectable absorbance of 0.002, as illustrated in Figure 13, and a maximum absorbance of 2, which was chosen as a safely detectable maximum. Minimum detection limits at 1 atm are 400 ppb/m at room temperature and 10 ppm/m at 3500 K for 1 kHz detection bandwidth.

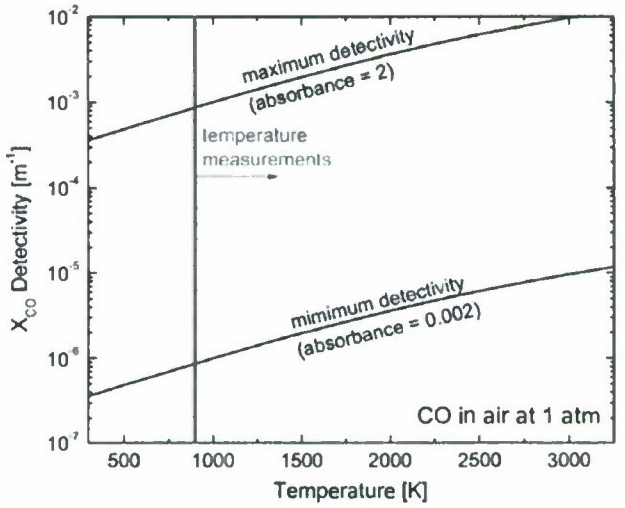

Figure 18. CO detection limits and range of sensitive temperature measurements for developed sensor at a pressure of 1 atm.

In addition to the atmospheric pressure shock tube CO and thermometry measurements described above, measurements were made using the same scanned-wavelength techniques at slightly elevated pressures (4-5 atm). An example absorbance trace is illustrated in Figure 19 with comparison to spectral simulation. The sensor measured temperature and CO mole fraction are 1857 K and 0.98% which compare well to reflected shock conditions of 1870±13 K and 1.00±0.01% CO, respectively.

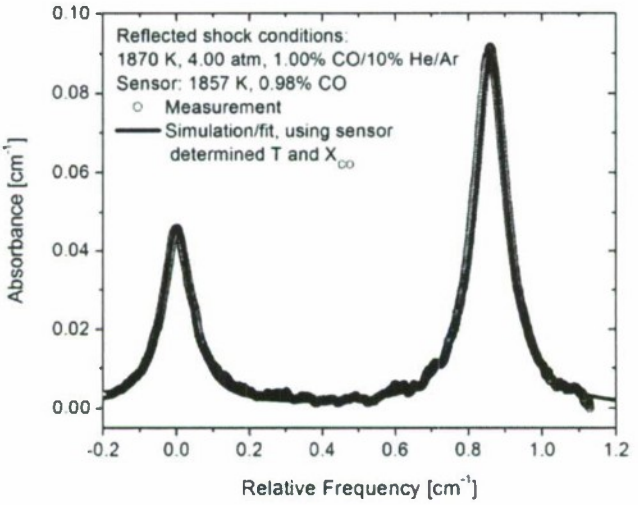

Figure 19. Example 4 atm high-temperature CO absorbance measurements and fit simulation for the R(10) and R(18) transitions.

Measurements, as illustrated in Figure 19, have been made from 1350 to 2275 K at 4-5 atm with relatively good agreement between measured temperature and the reflected shock conditions (1σ

deviation of ±2.1%) as illustrated in Figure 20. Spectral simulations indicate that measurements upwards of 20 atm are possible but that at pressures much beyond 20 atm the blending the spectral lines become too significant to discriminate the features for thermometry.

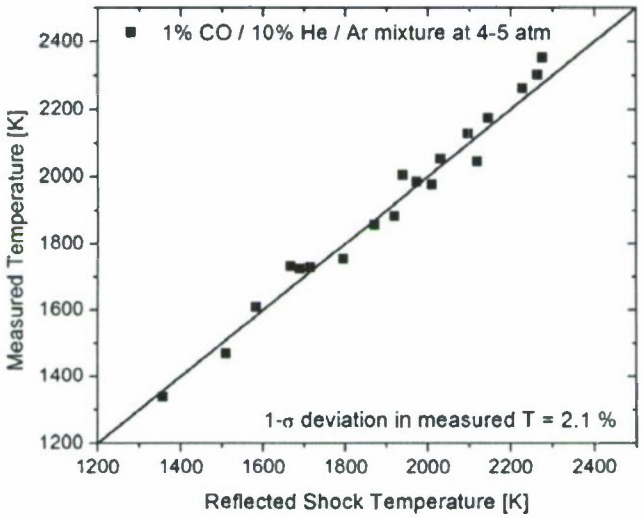

Figure 20. Temperature measurements for shock tube experiments performed at 4-5 atm.

5.3 Flat Flame Measurements

For demonstration of the sensor in a combustion environment, scanned-wavelength absorption measurements were made in atmospheric pressure premixed ethylene/air flat flames supported on a McKenna burner for equivalence ratios ranging from 0.7 to 1.4. Two-line scanned-wavelength measurements provided temperature and CO determinations, in the same manner and using the same techniques demonstrated in the shock tube experiments, and were compared to thermocouple temperature measurements and chemical equilibrium predictions for CO at the measured temperatures.

Similar to many flat flame laser absorption demonstrations [47-48], thermocouple measurements were made to determine the level of temperature spatial uniformity across the laser line-of-sight and to provide a comparison for the sensor results. Corrections were made to the raw thermocouple readings using the recommendations of Shaddix [49]. The correction model (officially the Ranz and Marshall correlation [50]) accounts for radiation losses and convective heating for the thermocouple, the emissivity of the thermocouple at flame temperatures, the thermocouple geometry dependence on radiation and convective heat transfer, temperature dependence of the gas-phase thermal conductivity, and Reynolds number affects. These corrections resulted in an addition to the raw

thermocouple readings of 36 K at an ethylene/air equivalence ratio Φ = 0.5, an addition of 75 K at Φ = 1.0, and an addition of 65 K at Φ = 1.5.

All thermocouple and sensor measurements were made at a location 1.5 cm above the burner, chosen because lower heights above the burner suffered from lower spatial uniformity and greater heights from heat loss to the surroundings. A height of 1.5 cm for McKenna burner optical measurements has also been used by several authors in the literature [47,51-52].

The temperature across the center portion of the flame varies by 30-50 K, depending on equivalence ratio, likely due to abnormalities in the porous burner surface. There is a steep gradient in temperature at the flame edge where the flame temperature varies from the average flat-flame value to less than 1000 K in ~5 mm of distance. Note, that the path length of hot gases for laser absorption measurements varies depending on the operating equivalence ratio, for the Φ = 0.5 case the flat flame portion is 17% shorter than at Φ = 1.0. See Figure 21 for thermocouple-measured flame temperature profiles.

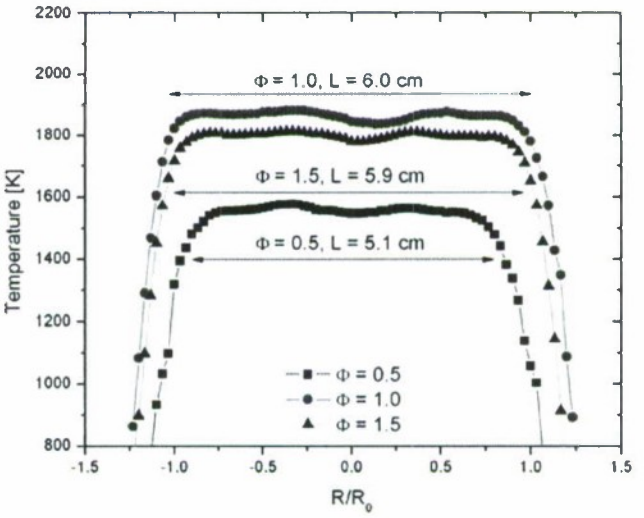

Figure 21. Themocouple measurements of flat flame temperature profiles at a distance 1.5 cm from the McKenna burner surface.

To account for the path length of hot gases, which is shorter than the burner diameter, an effective path length was used for all sensor temperature measurement which was defined as the path for which the temperature was above 95% of the mean core temperature. This definition of effective path length is arbitrary but not of significant sensitivity for temperature measurements due to the reasonably steep drop off in temperature at the flame edge. However, there are some complications when simultaneously determining temperature and CO concentration due to differences in effective

path length for the two parameters. As described by Schoenung and Hanson [47], in fuel-rich flames the colder products at the flame edge result in lower equilibrium levels of CO at the edge, due to the dependence of chemical equilibrium on temperature at fuel-rich conditions. On the other hand, in fuel-lean flames the colder products cause CO concentrations in excess of equilibrium at the flame edge, due to incomplete oxidation of the fuel resulting from low temperatures and correspondingly low levels of radical species (e.g., OH) to complete the oxidation from CO to CO_2.

Direct-absorption scanned-wavelength measurements were made at 1 kHz scan rates in flat flames produced by the McKenna burner similarly to those made in the high-temperature shock tube studies. Measurements were limited to a range of equivalence ratios from 0.7 to 1.4 due to insufficient absorption in leaner flames and optically thick conditions in richer flames. For thermometry measured peak absorbance ratios for the R(10) and R(18) lines were compared to spectral simulations at 1 atm for a best fit of the peak absorbance ratio, air was assumed to be the sole colliding gas. The assumption of air as the sole colliding gas causes slightly narrower line widths in simulation when compared to measurement but this should cancel out to some degree in the peak absorbance ratio-based temperature determinations. Once the temperature was determined the CO mole fraction was determined from the peak absorbance measured for the two features.

An example absorbance trace measured in an $\Phi = 1.2$ ethylene/air flame is shown in Figure 22 with comparison to a HITRAN spectral simulation at the sensor determined conditions; this measurement is the result of a single 1 kHz scan and involves no averaging which is contrary to much of the literature [47-48,51-52] where flame measurements have been reported after multiple-scan averaging to increase the signal-to-noise ratio. In this case the thermocouple measured core flame temperature is 1867 K and the sensor measured temperature is 1874 K illustrating excellent agreement, as was the case for all stoichiometric to rich experiments. Also, the thermocouple temperature can be used to predict the product gas composition under the assumption of chemical equilibrium. For this $\Phi = 1.2$ ethylene/air flame the chemical equilibrium CO concentration is 5.56% and that measured by the sensor is 5.80%.

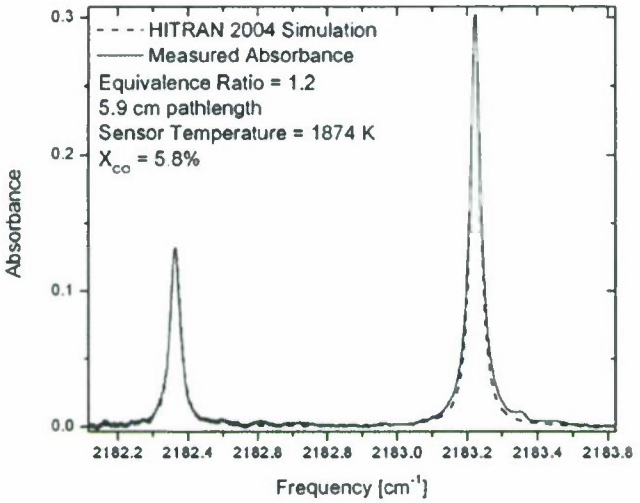

Figure 22. Example absorbance measurement for the R(10) and R(18) lines with overlaid HITRAN 2004 [5] simulation for atmospheric pressure Φ = 1.2 ethylene/air flat-flame.

See Figure 23 for the comparison of all sensor temperature and thermocouple measurements and Figure 24 for comparison of sensor CO mole fraction measurements and chemical equilibrium predictions for CO mole fraction. The comparison between sensor temperature and CO mole fraction measurements and thermocouple temperature measurements and chemical equilibrium predictions for CO using the thermocouple measurements are excellent for equivalence ratios from stoichiometric to Φ = 1.4. In fact the temperature measurements are well within the estimated sensor and thermocouple uncertainties, indicating that both are likely over predicted at these conditions. The excellent agreement is due to several interrelated reasons. First, the high CO concentrations allow very high signal-to-noise ratios. Second, the rich conditions create a flat temperature profile with a very sharp drop off at the flame edge. In the sharp cool edge of the rich flame there is less CO in the product gases than in the flame core, causing less absorption in the flame edge than the core and a very well defined top-hat CO profile. Finally, the product composition of rich flames at the equivalence ratios studied is, for all practical purpose, in chemical equilibrium. Hence, the rich conditions create a direct comparison between thermocouple, chemical equilibrium, and sensor and the agreement is excellent.

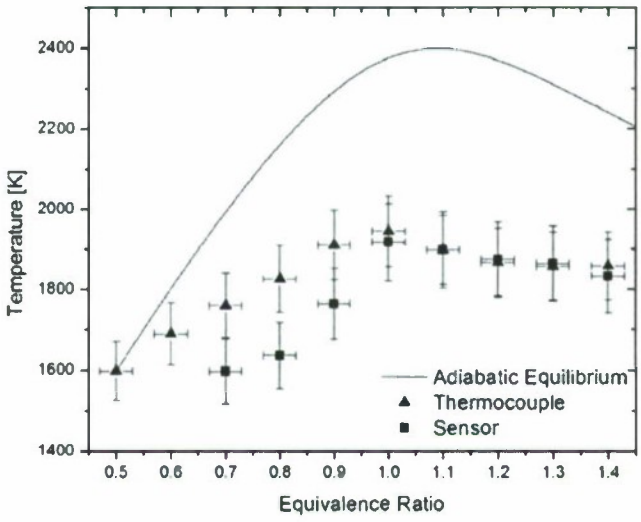

Figure 23. Atmospheric pressure ethylene/air flat-flame thermocouple core gas temperature measurements (1.5 cm above burner surface) and line-of-sight scanned-wavelength laser absorption sensor measurements (1.5 cm above burner surface).

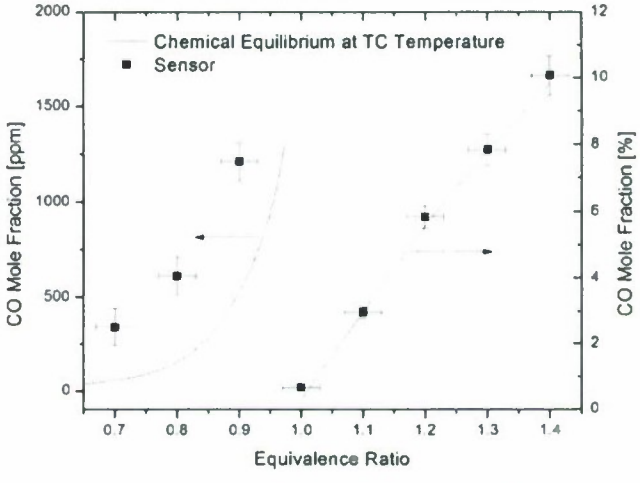

Figure 24. Atmospheric pressure ethylene/air flat-flame chemical equilibrium predictions at the measured thermocouple temperature and scanned-wavelength sensor measured CO mole fractions (1.5 cm above burner surface).

On the other hand, measurements made in lean ethylene/air flames show some deviation between sensor measurements, thermocouple temperatures, and chemical equilibrium predictions. The observed differences are due to the influence of the flame edge on lean flames. At the flame edge, under lean conditions, the temperature drops off more gradually than in the rich case. This provides a shorter path length of high-temperature gases near chemical equilibrium, those which are probed by the thermocouple. These colder product gases at the flame edge do not allow complete oxidation of CO

to CO_2. Hence, in the cool flame edge the CO concentrations are in excess of those predicted by equilibrium, as previously shown through flame sampling [47] and indicated by the line-of-sight-averaged sensor measurements here. In addition, not only are the CO concentrations greater in the flame edge but the sensor magnifies their influence because these higher concentrations occur at temperatures lower than those in the flame core. This results in greater absorption in the low-temperature R(10) line and less absorption in the high-temperature R(18) line, which not only causes a lower sensor temperature result than that given by the thermocouple but also increases the amount of integrated CO measured by the sensor using the low-temperature line. In other words, there are two effects, higher cold-edge CO concentrations and preferential and stronger absorption in the low-temperature line in the flame edge, which result in non-linear perturbations of the sensor-measured temperature down and sensor-measured CO up. These observations for lean premixed flat-flames have been made previously [47-48] and are not indicative of problems with sensor measurements but indicate that care must be taken when interpreting laser absorption signals and that chemical equilibrium assumptions are not always justified and can result in discrepancies for flame products and emissions.

6. Wavelength-Modulation Sensor Demonstrations

6.1 Low-Temperature Gas Cell Measurements

For WMS sensor demonstration, measurements were first carried out in a room-temperature gas cell (10 cm path length) for specified CO containing mixtures. Both the low-temperature R(9) and R(10) lines were probed to test the linearity of 1*f* normalized WMS-2*f* peak heights with increasing CO concentration in CO/N_2 mixtures and to investigate the signal-to-noise ratio (SNR) differences between sensor operation in scanned-wavelength and WMS modes. Because for fixed modulation depth, WMS-2*f* peak height will vary with temperature, pressure, and the concentration of the absorber, room-temperature measurements at fixed initial pressure were chosen to simplify these interdependences. The laser was operated at the high-temperature operating point (modulation frequency f = 50 kHz, modulation depth a = 0.04 cm^{-1}) for a scan rate (detection bandwidth) of 1 kHz and a lock-in amplifier bandwidth of 15 kHz. Operation using these input parameters is far from optimal for room-temperature measurements where the line widths are substantially greater than they are at high temperatures. However, we chose to use these operating parameters for consistency with the thermometry measurements presented next and wish to point out that optimization of the QCL modulation for room-

temperature measurements would result in greater improvement in SNR in comparison to direct-scanned-wavelength absorption than is shown here.

Results for 1*f* normalized WMS-2*f* peak heights for a range of CO mole fractions varying from 10 to 220 ppm of CO in 500 Torr of N_2 are shown in Figure 25, illustrating linearity and demonstrating the utility of the sensor for CO measurements. In Figure 26 a raw WMS-2*f* line shape is shown along with comparison to a scanned-wavelength direct-absorption line shape measurement (same as Figure 13) for a mixture containing 17 ppm of CO in 430 Torr of argon (10 cm path length). The comparison illustrates an increase in the SNR of almost an order-of-magnitude for the WMS measurement relative to scanned-wavelength. In the scanned-wavelength case the CO detection limit is 0.24 ppm per meter of path length at the given conditions (297 K and 430 Torr) for a 1 kHz detection bandwidth. While, in the WMS case the CO detection limit is 0.03 ppm per meter of path length at the same conditions and detection bandwidth. Additionally, the noise characteristics are quite different for the two measurements. The scanned-wavelength direct absorption measurement is dominated by high-frequency noise emanating from the laser and detector and the WMS measurement only exhibits low-frequency noise that was generated in the lock-in-amplification mixer and passed through the lock-in low-pass filter.

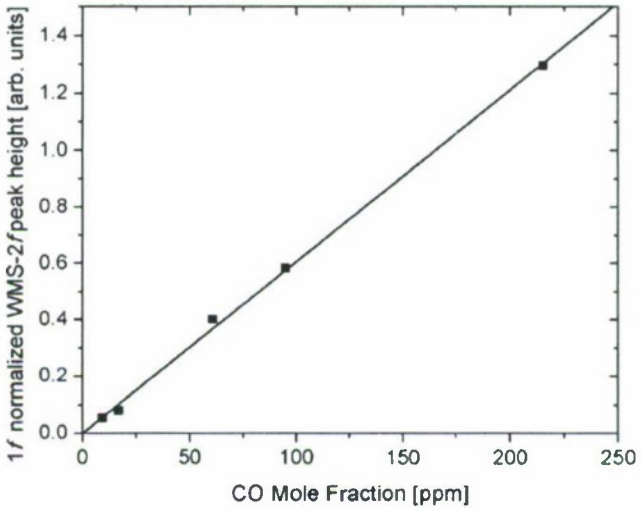

Figure 25. Measured 1*f* normalized WMS-2*f* peak heights for the R(9) line for 500 Torr CO/N_2 mixtures, where the CO mole fraction varies from 10 to 220 ppm.

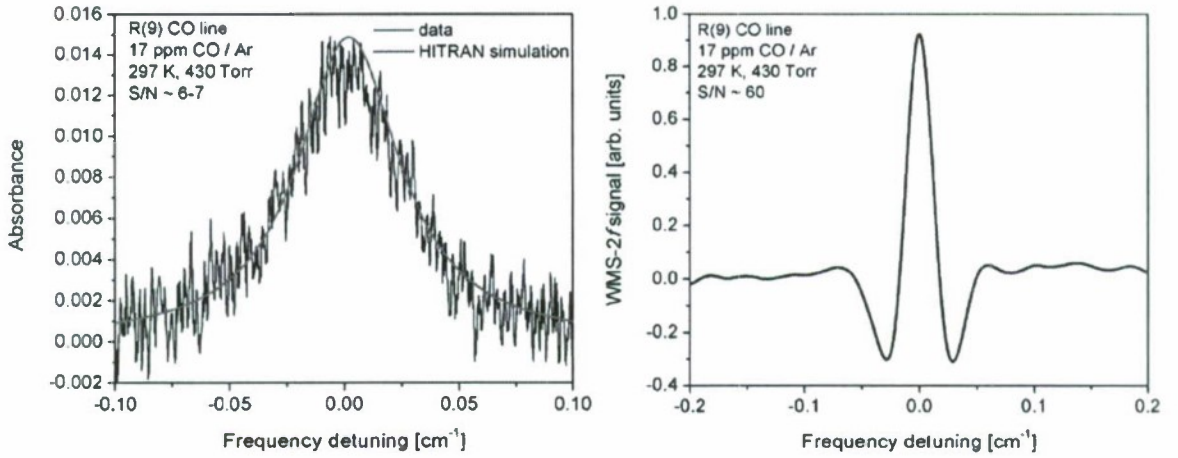

Figure 26. Line shape measurements made for the R(9) CO line using scanned-wavelength direct absorption (left) and the WMS-2*f* technique (right) for a 430 Torr mixture containing 17 ppm of CO in argon.

6.2 High-Temperature Shock Tube Measurements

For demonstration of the QCL WMS sensor for thermometry, measurements were performed in reflected-shock-heated gases, again in a shock tube previously described by Moss et al. [46] (12.3 cm diameter and absorption path length). Measurements of both 1*f* and 2*f* line shapes were made at 500 Hz and 1 kHz scan rates (detection bandwidths) for either the R(9) and R(17) line pair or the R(10) and R(18) line pair in a given experiment. Using the ratio of the 1*f* normalized WMS-2*f* peak heights for a line pair allowed for temperature determinations, as described in section 3.2. For all of these measurements the QCL was modulated at 50 kHz and at a modulation depth of 0.04 cm^{-1} and the lock-in amplifier low-pass filter was set to 15 kHz.

Figure 27 illustrates an example shock tube thermometry measurement. In this case a mixture containing 0.05% CO, 10% He, and with argon making up the balance has been reflected-shock heated to 1582 K and 1.21 atm, conditions which were determined via the normal-shock relations and measurement of the incident shock velocity and have uncertainties (2σ) of ±0.7% and ±1.0%, for temperature and pressure respectively. Again, as in the scanned-wavelength measurements, helium was added to the mixtures to accelerate vibrational relaxation of the CO to ensure that a vibrationally relaxed condition was achieved within a few microseconds of shock passage. In this example the R(9) and R(17) lines were probed at a scanning rate of 500 Hz. The measured pressure (piezoelectric transducer) and the measured WMS-1*f* and WMS-2*f* line shapes are shown in Figure 27. The figure illustrates that the reflected shock test time, the time for which the pressure is relatively flat following the two-step rise associated with incident and reflected shock heating and prior to the slower decline due to expansion waves emanating from the shock tube driver section, is around 2.5 ms, allowing for

one complete scan of both the R(9) and R(17) lines at the 500 Hz scan rate within the test time. During the test time the temperature and pressure are nearly constant and homogenous providing an ideal environment for the demonstration of this sensor for thermometry. To extract temperature the measured 1*f* and 2*f* signals, as shown in Figure 27, were treated using the equations and methods laid out in section 3.2 resulting in a sensor determination for the temperature of 1588 K, in excellent agreement with the reflected shock condition (1582 K).

The results of thermometry measurements made around 1 atm, for 500 Hz and 1 kHz detection bandwidths, for CO/He/Ar mixtures where the CO mole fraction ranged from 100 ppm to 0.5% and the He mole fraction was kept fixed at 10%, and for a large range of temperatures (850-3500 K) are shown in Figure 28. The sensor measured temperatures agree well with the reflected shock temperatures, calculated using the normal-shock equations from the incident shock velocity, resulting in a 1σ standard deviation between sensor temperatures and reflected shock temperatures of ±1.9%. Importantly, these temperature measurements, made using the ratio of 1*f* normalized WMS-2*f* peak heights, do not require calibration. Additionally, thermometry measurements made using two lines with similar pressure broadening parameters, as is the case here, are fairly insensitive to operation at off-optimum modulation depths, as previously discussed and illustrated previously in Figure 8, which infers that the technique is fairly insensitive to measurements at pressures that deviate slightly from that expected, as is the case here where the reflected shock pressures deviate from 0.9 to 1.3 atm.

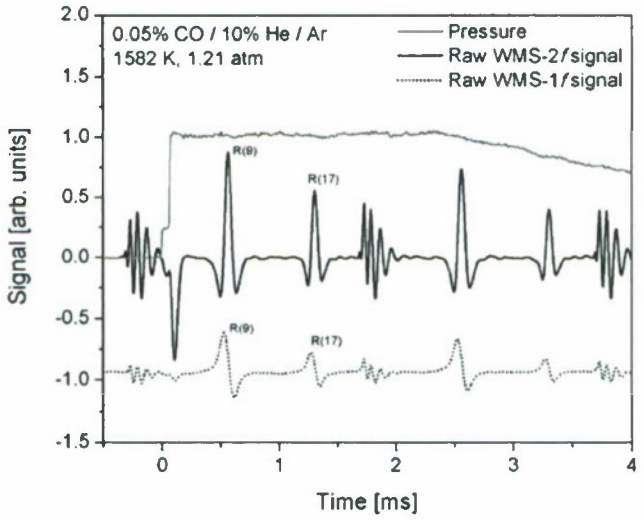

Figure 27. Example high-temperature shock tube thermometry measurement. Measured pressure and raw WMS-2*f* and WMS-1*f* signals are shown for sensor operation at a 500 Hz scan rate (detection bandwidth). Reflected shock conditions are: 0.05% CO/10% He/Ar, 1582 K, 1.21 atm (12.3 path length).

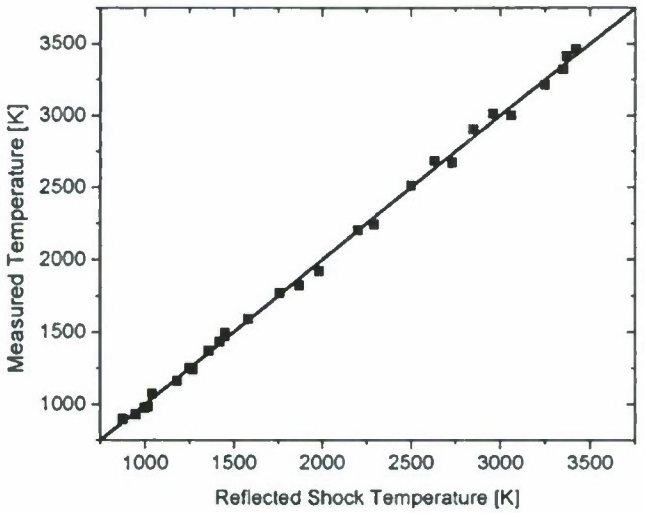

Figure 28. Shock tube thermometry sensor measurements compared the reflected shock temperature, calculated using the normal-shock relations and the measured incident shock velocity. Measurements were made for both the R(9) and R(17) and R(10) and R(18) line pairs and at both 500 Hz and 1 kHz. Mixtures varied from 100 ppm CO to 0.5% CO in bath gases containing 10% He with a balance of Ar.

7. Summary

A mid-IR (4.59 μm) QCL absorption sensor for sensitive measurements of CO and temperature has been developed. The sensor can be operated in either scanned-wavelength direct-absorption mode or in wavelength-modulation absorption spectroscopy mode, for enhanced sensitivity. Demonstration and validation measurements have been made in a room temperature gas cell, a shock tube at high-temperature conditions, and a flat flame. In direct-absorption mode at a detection bandwidth of 1 kHz, the sensor is capable of sensitive thermometry for a very large range of temperatures (950-3500 K demonstrated here) and provides CO detection with detection limits at 1 atm of 400 ppb per meter of absorption path length room temperature and 10 ppm per meter of absorption path length at 3500 K. In WMS mode the sensor, is capable thermometry at a similarly large range of temperatures and exhibits CO detection limits around an order-of-magnitude smaller. To the PI's knowledge, this work demonstrates the first use of a mid-IR QCL-based absorption sensor for thermometry at combustion-like temperatures.

8. Participating Personnel

Principle Investigator
Prof. Matthew Oehlschlaeger

Graduate Students
Jeremy Vanderover, Ph.D received 2010 under this grant, currently at General Electric Research Center, Niskayuna, NY
Andrew Berkowitz, M.S. received 2010, currently at SpaceX, McGregor, TX
Nicholas Herrick-Kaiser, M.S. received 2008, currently at Ametek, Woodstock, NY
Weijing Wang, Ph.D. in progress

9. Publications

1. J. Vanderover and M.A. Oehlschlaeger, "A Mid-Infrared Scanned-Wavelength Laser Absorption Sensor for Carbon Monoxide and Temperature Measurements from 900 to 4000 K," *Applied Physics B* 99, 353-362 (2010).
2. J. Vanderover, W. Wang, and M.A. Oehlschlaeger, "A Carbon Monoxide and Thermometry Sensor Based on Mid-IR Quantum-Cascade Laser Wavelength-Modulation Absorption Spectroscopy," *Applied Physics B*, in review.
3. A.M. Berkowitz and M.A. Oehlschlaeger, "The Photo-Induced Ignition of Quiescent Ethylene/Air Mixtures Containing Suspended Carbon Nanotubes," *Proceedings of the Combustion Institute* 33, 3359-3366 (2011).

10. References

1. K. Kohse-Höinghaus, J.B. Jeffries, "Applied Combustion Diagnostics," Taylor and Francis, New York (2002).
2. M.G. Allen, Meas. Sci. Technol. 9, 545 (1998).
3. R.K. Hanson, P.A. Kuntz, C.H. Kruger, Appl. Opt. 16, 2045 (1977).
4. R.K. Hanson, P.K. Falcone, Appl. Opt. 17, 2477 (1978).
5. L. S. Rothman, D. Jacquemart, A. Barbe, D. Chris Benner, M. Birk, L. R. Brown, M. R. Carleer, C. Chackerian Jr., K. Chance, L. H. Coudert, V. Dana, V. M. Devi, J.-M. Flaud, R. R. Gamache, A. Goldman, J.-M. Hartmann, K. W. Jucks, A. G. Maki, J.-Y. Mandin, S. T. Massie, J. Orphal, A. Perrin, C. P. Rinsland, M. A. H. Smith, J. Tennyson, R. N. Tolchenov, R. A. Toth, J. Vander Auwera, P. Varanasi, G. Wagner, J. Quant. Spectrosc. Rad. Trans. 96, 139 (2005).
6. J. Faist, F. Capasso, D.L. Sivco, C. Sirtori, A.L. Hutchinson, A.Y. Cho, Science 22, 553-556 (1994).
7. J. Faist, Opt. Photonics News 17, 32 (2006).
8. F. Capasso, R. Paiella, R. Martini, R. Colombelli, C. Gmachl, T.L. Myers, M.S. Taubman, R.M. Williams, C.G. Bethea, K. Unterrainer, H.Y. Hwang, D.L. Sivco, A.Y. Cho, A.M. Sergent, H.C. Liu, E.A. Whittaker, IEEE J. Quantum Elect. 38, 511 (2002).
9. A.A. Kosterev, F.K. Tittel, R. Köhler, C. Gmachl, F. Capasso, D.L. Sivco, A.Y. Cho, S. Wehe, M.G. Allen, Appl. Opt. 41, 1169 (2002).
10. F.K. Tittel, D. Weidmann, C. Oppenheimer, L. Gianfrani, Opt. Photonics News 17, 24 (2006).
11. Y.A. Bakhirkin, A.A. Kosterev, C. Roller, R.F. Curl, F.K. Tittel, Appl. Opt. 43, 2257 (2004).
12. C. Roller, K. Namjou, J.D. Jeffers, M. Camp, A. Mock, P.J. McCann, J. Grego, Appl. Opt. 41, 6018 (2002).
13. Q. Shi, D.D. Nelson, J.B. McManus, M.S. Zahniser, M.E. Parrish, R.E. Baren, K.H. Shafer, C.N. Harward, Anal. Chem. 75, 5180 (2003).

14. S. Wehe, M. Allen, X. Liu, J. Jeffries, R. Hanson, AIAA Paper AIAA-2003-588 (2003).
15. S. Wehe, M. Allen, X. Liu, J. Jeffries, R. Hanson, Proc. IEEE Sens. 2, 295 (2003).
16. G. Wysocki, A.A. Kosterev, F.K. Tittel, Appl. Phys. B 80, 617 (2005).
17. X. Chao, J.B. Jeffries, R.K. Hanson, Proc. Combust. Inst. 33, doi:10.1016/j.proci.2010.05.014.
18. L.C. Philippe, R.K. Hanson, Appl. Opt. 32, 6090 (1993).
19. H. Li, A. Farooq, J.B. Jeffries, R.K. Hanson, Appl. Phys. B 89, 407 (2007).
20. A. Farooq, J.B. Jeffries, R.K. Hanson, Appl. Phys. B 90, 619 (2008).
21. A. Farooq, J.B. Jeffries, R.K. Hanson, Appl. Phys. B 96, 161 (2009).
22. A.Y. Chang, E.C. Rea, R.K. Hanson, Appl. Opt. 26, 885 (1987).
23. M.A. Oehlschlaeger, D.F. Davidson, J.B. Jeffries, Appl. Opt. 44, 6599 (2005).
24. J.M. Hollas, "High Resolution Spectroscopy, 2nd Edition," Wiley, New York (1998).
25. F. Thibault, R.Z. Martinez, J.L. Domenech, D. Bermejo, J.-P. Bouanich, J. Chem. Phys. 117, 2523 (2002).
26. A.W. Mantz, V.M. Devi, D.C. Benner, M.A.H. Smith, A. Predoi-Cross, M. Dulick, J. Mol. Struct. 742, 99 (2005).
27. R. Farrenq, G. Guelachvili, A. J. Sauval, N. Grevesse, C. B. Farmer, J. Mol. Spectrosc. 149, 375 (1991).
28. N. Authier, N. Bagland, A. LeFloch, J. Mol. Spectrosc. 160, 590 (1993).
29. D. Goorvitch, Astrophys. J. Suppl. Ser. 95, 535 (1994).
30. L.A. Young, W.J. Eachas, J. Chem. Phys. 44, 4195 (1966).
31. L.A. Young, J. Quant. Spect. Rad. Trans. 8, 693 (1968).
32. C. Chackerian Jr., R. H. Tipping, J. Mol. Spectrosc. 99, 431 (1983).
33. Q. Zou, P. Varanasi, J. Quant. Spect. Rad. Trans. 75, 63 (2002).
34. R.H. Hunt, R.A. Toth, E.K. Plyer, J. Chem. Phys. 49, 3909 (1968).
35. D.A. Draegert, D. Williams, J. Opt. Soc. Am. 58, 1399 (1968).
36. P.M. Sinclair, P. Duggan, R. Berman, A.D. May, J.R. Drummond, J. Mol. Spectrosc. 181, 41 (1997).
37. P.M. Sinclair, P. Duggan, R. Berman, J.R. Drummond, A.D. May, J. Mol. Spectrosc. 191, 258 (1998).
38. A. Predoi-Cross, C. Luo, P.M. Sinclair, J.R. Drummond, A.D. May, J. Mol. Spectrosc. 198, 291 (1999).
39. G.V.H. Wilson, J. Appl. Phys. 34, 3276 (1963).
40. R. Arndt, J. Appl. Phys 36, 2522 (1965).
41. J. Reid, D. Labrie, Appl. Phys. B 26, 203 (1981).
42. H. Li, G.B. Rieker, X. Liu, J.B. Jeffries, R.K. Hanson, Appl. Opt. 45, 1052 (2006).
43. P. Kluczynski, O. Axner, Appl. Opt. 38, 5803 (1999).
44. D.D. Nelson, J.B. McManus, S.C. Herndon, J.H. Shorter, M.S. Zahniser, S. Blaser, L. Hvozdara, A. Muller, M. Giovannini, J. Faist, Opt. Lett. 31, 2012 (2006).
45. A.A. Kosterev, A.L. Malinovsky, F.K. Tittel, C. Gmachl, F. Capasso, D.L. Sivco, J.N. Baillargeon, A.L. Hutchinson, A.Y. Cho, App. Opt. 40, 5522 (2001).
46. J.T. Moss, A.M. Berkowitz, M.A. Oehlschlaeger, J. Biet, V. Warth, P.A. Glaude, F. Battin-Lecerc, J. Phys. Chem. A 112, 10843 (2008).
47. S.M. Schoenung, R.K. Hanson, Combust. Sci. Technol. 24, 227 (1981).
48. J. Wang, M. Maiorov, D.S. Baer, D.Z. Garbuzov, J.C. Connolly, R.K. Hanson, Appl. Opt. 39, 5579 (2000).
49. C. R. Shaddix, "Correcting thermocouple measurements for radiation loss: A critical review" Proceedings of the 33rd National Heat Transfer Conference. paper HTD99-282 (1999).
50. W. E. Ranz, W. R. Marshall Jr., Chem. Eng. Prog. 48, 141 (1952).
51. W. Clauss, V.I. Fabelinsky, D.N. Kozlov, V.V. Smirnov, O.M. Stelmakh, K.A. Vereschagin, Appl. Phys. B 70, 127 (2000).
52. M. E. Webber, S. Kim, S. T. Sanders, D. S. Baer, R. K. Hanson, Y. Ikeda, Appl. Opt. 40, 821 (2001).

A. Appendix: The Photo-Ignition of Quiescent Fuel/Air Mixtures Containing Suspended Carbon Nanotubes

Described in this appendix is an investigation of the use of photo-sensitive nanomaterials to photo-ignite gaseous fuel/air mixtures. This work, although not part of our proposal or related to laser sensing, is nonetheless of intrinsic interest to combustion and propulsion and was included as part of the overall project.

A.1. Introduction

In 2002 Ajayan et al. [1] accidently discovered that single-wall carbon nanotubes (SWCNTs) ignite in air when exposed to an ordinary camera flash. They found that ignition occurred for "as-prepared" (no purification) SWCNTs made using carbon arc, laser ablation, or chemical vapor deposition methods when synthesized on Ni-Y or Fe catalyst. Following the camera flash, SWCNT samples ignited producing temperatures estimated between 1500 and 2000 °C by Ajayan et al., based on structural changes to the nanotube samples. It was also observed that only as-prepared SWCNTs were easily ignited; multi-walled carbon nanotubes, graphite powder, fluffy carbon soot, and C_{60} did not ignite. Other important observations from the Ajayan et al. study were that the optical power required for photo-ignition of the SWCNTs with metal impurity was quite low, in the range of 100-300 $mWcm^{-2}$, and that the photo-ignition was stronger for samples with lower density (more segmentation or distribution), which the authors postulate was due to a reduction of conduction losses from ignition points to the bulk material. Ajayan et al. hypothesized that the radiative energy from the camera flash is absorbed and confined in the SWCNT structure which causes fission and then oxidation of the nanotube structure, in turn providing high temperatures, allowing oxidation of the metal catalyst nanoparticle.

Following the initial work by Ajayan et al., others have investigated this phenomenon including Bockrath et al. [2] who showed that the phenomenon is not isolated to SWCNTs but in fact other carbonaceous compounds synthesized on metal catalysts can ignite upon exposure to a flash lamp and Braidy et al. [3] who through x-ray powder diffraction and transmission electron microscope (TEM) analysis showed that iron oxides, Fe_2O_3 and Fe_3O_4, were present in the products of the flash ignition of SWCNTs with Fe impurity and that the Fe_2O_3 had undergone melting, indicating temperatures of at least around 1500 °C had be achieved.

Smits et al. [4] repeated the SWCNT ignition experiments of Ajayan et al. and also showed that Fe powder (particles with diameters of 6-10 μm) ignites when exposed to a camera flash but that SWCNTs purified with acid do not. Based on this observation, Smits et al. concluded that the metal

nanoparticle impurities in the SWCNT samples are responsible for the photo-ignition phenomenon. Smits et al. postulated that photons from the camera flash are absorbed by the catalytic metal nanoparticles resulting in confined thermal energy and very high temperatures (the thermal conductivity of Fe nanoparticles is ~80 W/m/K while the thermal conductivity for the SWCNTs is ~66,000 W/m/K which allows for more rapid dissipation of absorbed energy in the SWCNTs relative to that absorbed by the Fe nanoparticles) which causes the Fe nanoparticles to oxidize forming mostly Fe_2O_3 and, in turn, causes ignition and burning of the SWCNTs and structural modifications (i.e., fusing) to adjacent SWCNTs. Smits et al. argued that the ignition observed in SWCNTs is in fact due to the oxidation of the metal nanoparticle impurities and the SWCNTs act simply to stabilize the pyrophoric metal nanoparticles until they are exposed to the light stimulus.

The work of both Braidy et al. [3] and Smits et al. [4] describes in detail the structure of SWCNTs and Fe nanoparticle impurities before and after flash ignition providing foundation for the theory put forward by Smits et al. and backing to the claims of high temperatures (1500 °C and up) during SWCNT ignition. By way of TEM images of unpurified as-produced SWCNTs, Braidy et al. determined that their un-flashed samples contained 23% Fe nanoparticles by weight prior to ignition and through electron energy loss spectroscopy (EELS) they showed that the majority of the Fe material was bulk Fe and not various forms of iron oxides. Furthermore, the nanoparticle Fe material was found to be embedded inside the nanotube bundles, providing a means for stabilization of the Fe to oxidation. Through TEM measurements for the orange material which remained after the flashing of SWCNTs samples, Braidy et al. determined the molecular makeup of the Fe-containing portions of product material. Most of the material was found to be Fe_2O_3 with some small quantities of Fe_3O_4. The appearance of these two iron oxides indicates that temperatures in excess of 700 °C for the formation of Fe_2O_3 and 1500 °C in the formation of Fe_3O_4 were achieved. There was also the appearance of free-standing fused grains within the Fe_2O_3 nanostructures, indicating that melting and coalescence of Fe_2O_3 nanoparticles had occurred which requires temperatures near 1500 °C. These experiments agree with the estimated temperatures based on the energetic requirements for the reconstruction of the nanotube bundles as observed by Ajayan et al. [1].

Since these original studies, there have been several further investigations carried out related to the photo-ignition phenomenon for carbon nanotubes [5-8]. However to our knowledge, there have been only two applications of the photo-ignition phenomenon to combustion processes, where the high temperatures provided by the simple inexpensive low-power camera flash of light-sensitive nanomaterials have the obvious potential to ignite various fuel/oxidizer mixtures via traditional thermal

ignition induced by the hot photo-ignited nanomaterials. Chehroudi and Danczyk [9] demonstrated the ignition of a single liquid fuel droplet via SWCNT photo-ignition by mixing a droplet of liquid 2-hydroxyethylhydrazine nitrate (HEHN), a high-energy density ionic liquid fuel, with SWCNTs containing Fe impurities and exposing the droplet to a camera flash while flowing oxygen over the droplet, which resulted in the droplet igniting and burning. They reported that oxygen, rather than ambient air, was needed due to the low concentration of Fe in their partly-purified SWCNTs. Chehroudi and Danczyk also conceptualized [9] and patented [10-11] the idea of using carbon nanotubes for distributed ignition and suggested that the concept could be used for distributed ignition in rocket and internal combustion engine applications. The other combustion application of the photo-ignition of nanotubes, that the PI is aware of, is the demonstration of the initiation of solid explosives (K-6 and PETN (pentaerythritol tetranitrate)) by Manaa et al. [12] using flash exposure of SWCNTs containing Fe impurity.

The photo-ignition phenomenon, first discovered by Ajayan et al. [1], applied to the ignition of combustibles by Chehroudi and Danczyk [9] and Manaa et al. [12], and outlined above, offers an opportunity for the manipulation of combustion phenomena. The user-controlled on-demand photo-ignition of combustible mixtures containing photo-sensitive nanomaterials may allow for potential control over the time and location of chemical reaction which in turn may, for example, provide more rapid and homogeneous ignition and combustion, high-speed flame holding, rapid deflagration-to-detonation transition, and stable burning at very lean conditions.

The photo-ignition of nanomaterials for the induced ignition of combustible mixtures may provide an alternative to spark ignition, laser ignition, plasma ignition, plasma assisted/enhanced combustion, and catalytic nanomaterials for combustion enhancement, among others, with several potential advantages including lower power requirements than spark, laser, and plasma sources and lower cost and mass relative to laser and plasma sources. The photo-ignition phenomena results in on-demand ignition, with the particles achieving the high temperatures reported (~1500 °C) essentially instantaneously (~nanoseconds) relative to typical fluid mechanic and chemical time scales important in combustion processes. This has advantages over catalytic nanomaterials for combustion enhancement, which when distributed into a flow or combustion process are reliant on a diffusion of reactants and products at the particle surface, a slow process relative to the instantaneous and on-demand ignition via exposure to an external light source.

In the study described here it is demonstrated for the first time, to the PI's knowledge, that the photo-induced ignition of photo-sensitive nanomaterials (SWCNTs with Fe impurity) can be used to quasi-homogeneously ignite gaseous quiescent fuel/air mixtures.

A.2. Experimental Method

Experiments were carried out in a closed static combustion chamber to investigate the potential of SWCNT photo-ignition for the ignition of fuel/air mixtures and to compare the process with traditional automotive spark ignition. As-produced SWCNTs with 70% Fe impurity by weight, synthesized by Nano-C in a pre-mixed catalytic combustion process, were used in all reported experiments. A schematic of the combustion chamber is shown in Figure A.1. The combustion chamber is fitted with a Xe camera flash, piezoelectric pressure transducer, nanomaterial air-blast injector, automotive spark plug, optical window, and gas fill and vacuum line. The combustion chamber, fabricated from low-carbon steel, is cylindrical in geometry with an internal diameter of 50.8 mm and a length of 76.2 mm.

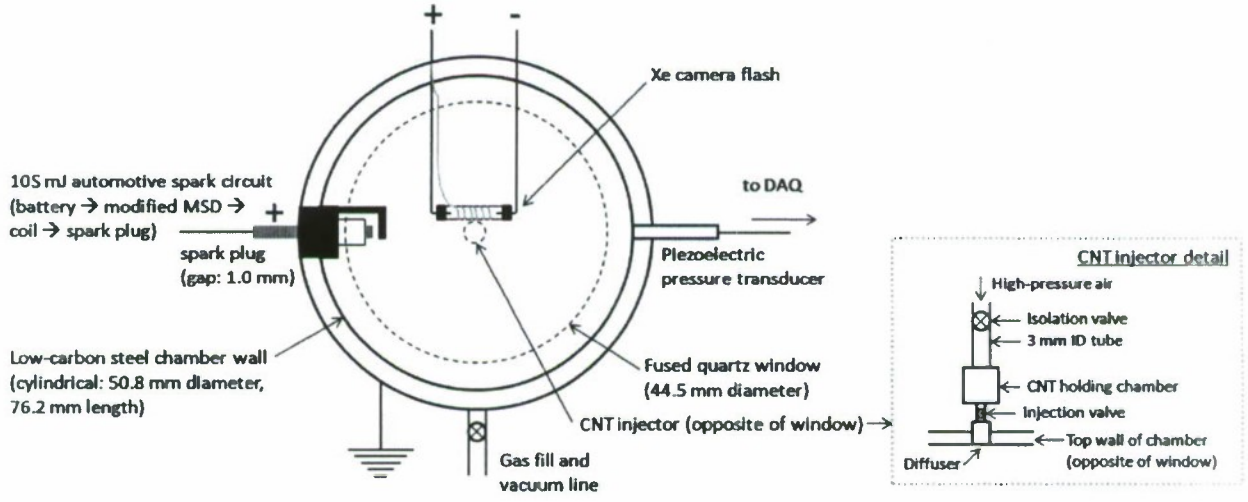

Figure A.1. Static combustion chamber experimental setup.

The Xe camera flash bulb is located inside and in the center of the combustion chamber with wires penetrating the cylindrical wall and insulated from the wall and sealed with epoxy. The Xe camera flash bulb and flash circuit (120 μF, 330 V capacitor) are from an unmodified Kodak disposable 35 mm camera (model 8951428-K) and is powered with a single 1.5 V AA battery. The Xe flash bulb has a color temperature of ~5800 K to emulate sunlight and is made of *borosilicate* to reduce ultraviolet output. See Figure A.2 for the flash emission spectrum measured in the visible region. At wavelengths shorter than 350 nm the spectrum decays quickly with little ultraviolet output due to the transmission characteristics of the borosilicate flash tube. At wavelengths longer than 800 nm the xenon emission spectrum is relatively flat, with some strong and distinct features around 900 nm, until around 2500 nm, beyond which the borosilicate does not transmit. The flash has a rise time of ~20 μs and flash duration of approximately 1 ms. At a standoff distance of 25 mm the flash produces peak output of ~120 $mWcm^{-2}$

and average output over the 1 ms flash duration of around ~40 $mWcm^{-2}$ as measured with a calibrated photodiode sensitive to a large wavelength region (200-5000 nm). It should be pointed out that while the energy stored in the capacitor for the Xe camera flash is high (~6.5 J), the flash is relatively inefficient in terms of luminous efficiency (~5% visible (400-700 nm) energy output to electrical energy input). The remainder of the input energy is lost due to non-ideal (incomplete) capacitor discharge, heating losses to the flash tube, the transmission characteristics of the borosilicate, or is at wavelengths outside of the visible region (much of the output is beyond 700 nm). Additionally, although the spectral characteristics of the photo-ignition process for nanomaterials is not yet well understood, presumably much of the long wavelength radiation is not useful for inducing the photo-ignition phenomenon. These issues are important to note for energetic considerations and the comparisons that are made here to the 105 mJ spark. Were the photo-ignition concept to find application, a better understanding of the optimal illumination wavelength and power requirements would be needed and a more efficient generation of optical output (e.g., light-emitting diode) would obviously be desired.

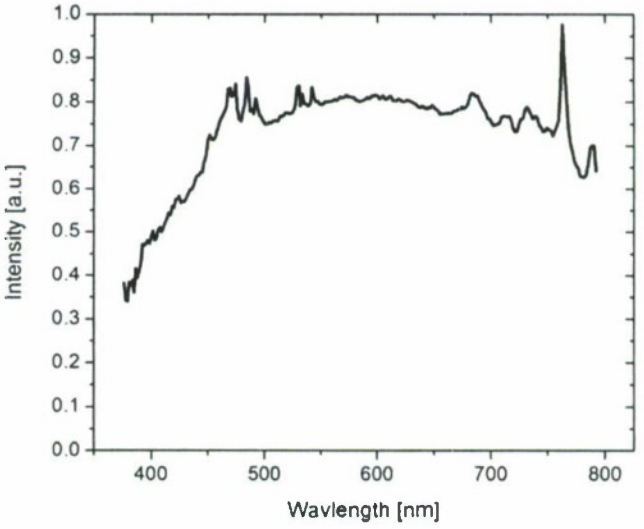

Figure A.2. Measured emission spectrum in the visible for the xenon camera flash (borosilicate flash tube) used in photo-ignition experiments. In the visible the flash is designed to mimic solar radiation (color temperature of 5800 K). At longer wavelengths the xenon emission is relatively flat with some distinct peaks around 900 nm and decays around 2500 nm due to decay in the borosilicate transmission beyond that point.

An automotive spark plug (Champion model RC12LC4, 1 mm gap) and piezoelectric pressure transducer (Dytran model 2300C3 transducer with model 4751B1 in-line charge amplifier and model 4120 signal conditioner, 1 μs rise time) are mounted in the cylindrical wall 180° opposite of each other and 90° from the wire penetration for the Xe camera flash. The spark plug protrudes into the chamber with the spark plug gap located 12 mm from the cylindrical wall; the face of the piezoelectric pressure transducer is

recessed 1 mm in the side wall and is coated with a thermal insulating silicone adhesive. The spark plug is powered by a standard automotive coil and spark plug wire which are energized by a MSD 6A capacitive discharge ignition controller, modified for single sparks, and powered by a 12 V automotive battery. The circuit produces single sparks with energy of ~105 mJ. An ammeter was placed around the spark plug wire for triggering data acquisition and determining the time of the spark.

Optical access is provided by a 6.35 mm thick fused quartz optic (44.5 mm optical diameter), flushed mounted into one of the flat faces of the chamber. The fused quartz optic allows for camera imaging of light emission and optical access for a photodetector used to trigger data acquisition at the time of the camera flash. A nanomaterial air-blast injection device is mounted in the center of the flat chamber wall opposite the fused quartz window. The injection device consists of an isolation valve, nanomaterial holding chamber, injection valve, and a diffuser which allows the flow to expand into the chamber aiding in the distribution of the nanotube suspension prior to ignition. The nanotubes were injected by first pressurizing the nanotube holding chamber with 90 psia air, isolating the holding chamber by shutting the isolation valve, following which the injection valve was opened allowing the nanotubes and injection air to flow through the diffuser (expanding geometry) into the chamber creating a quasi-distributed suspension of micrometer sized nanotube bundles, as can be observed in images found in Figure A.4. Although smaller sized bundles are desired, dispersing the SWCNTs, or for that matter any nanomaterial, down to nanometer-sized aggregates or single nanoparticles is extremely difficult without first suspending them in a liquid.

Both SWCNT photo-ignition and spark ignition (105 mJ) experiments were carried out for quiescent ethylene/air mixtures at an initial temperature of 297 K and initial pressures of 1 and 2 bar. Mixtures of ethylene and air were made via partial pressures in the combustion chamber by filling the evacuated chamber (ultimate pressure of 10^{-3} Torr) with gas from air (21±0.5% O_2 balance N_2) and ethylene (99.5% pure) high-pressure cylinders. Partial and total pressures were measured using a 1000 Torr Baratron capacitance manometer (±0.15% uncertainty) and a 50 psi Measurement Specialties pressure transducer (M5100 series, ±0.25% uncertainty). Mixtures were allowed to mix for 15 minutes prior to experiments to ensure homogeneity. For spark ignition experiments the quiescent ethylene/air mixtures were simply sparked to initiate data acquisition and combustion. For SWCNT photo-ignition experiments, the nanotubes were injected through the diffuser and then flashed within 1 second. The mass of air injected with the nanotubes was very small, approximately 0.7% of the initial chamber mass for 1 bar experiments and 0.35% for 2 bar experiments, and was accounted for in the determination of the initial mixture equivalence ratio. The mass of nanotubes placed in the holding chamber prior to a

given experiment was measured using a Mettler-Toledo AT 200 high-precision analytical balance. Losses of nanotubes in the injector device were small, as indicated by the lack of any visually observable nanotube material in the CNT holding chamber, injection valve, or diffuser. Experiments were performed for variations in injected nanotubes from 0.1 to 2 mg.

Measurements of dynamic pressure, made with the piezoelectric pressure transducer, were acquired for all experiments at a sample rate of 1 MHz and stored using a National Instruments DAQ card (PCI-6133) and LabVIEW software. For select experiments, images were obtained using a Redlake high-speed camera and associated software at a frame rate of 2 kHz with 30 μs exposure time.

Measured pressure traces for example SWCNT photo-ignition and spark ignition experiments are shown in Figure A.3 for a Φ = 0.7 ethylene/air mixture at an initial pressure of 2 bar. For the purposes of interpretation, the definitions of ignition delay time and ignition rise time were adopted from Wang et al. [13]. As displayed in Figure A.3, the ignition delay time is defined as the time interval from flash or spark to the time at which the change in pressure had risen to 10% of the peak change in pressure (peak ΔP in Figure A.3). The ignition rise time is defined as the time interval required for a transition in pressure from 10% to 90% of the peak ΔP. It can be clearly observed in the Figure A.3 example that the SWCNT photo-ignition process results in both shorter ignition delay and rise times as well as higher peak pressure.

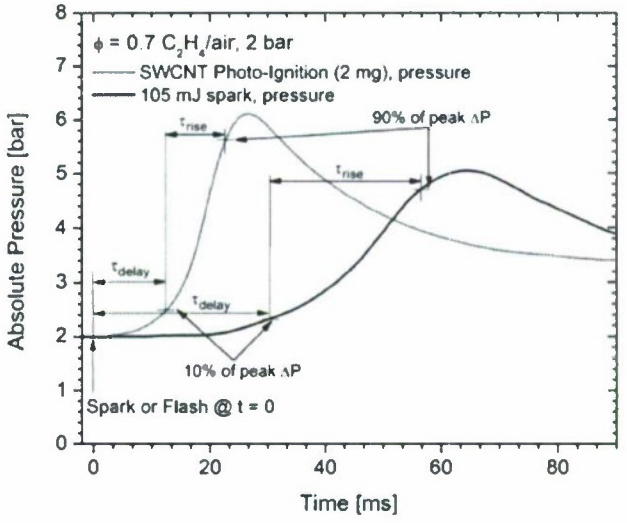

Figure A.3. Measured pressure for the SWCNT photo-ignition (2 mg of injected SWNCTs containing 70% Fe impurity by weight) and spark ignition (105 mJ) of a Φ = 0.7 C_2H_4/air mixture at an initial pressure of 2 bar.

A.3. Results and Discussion

a. Imaging

Camera images of unfiltered light emission were obtained at a frame rate of 2 kHz for both SWCNT photo-ignition and spark ignition for stoichiometric ethylene/air experiments at an initial pressure of 1 bar. The images for SWCNT photo-ignition are displayed in Figure A.4. In these images the flash occurs at t = 0 and decays through the first millisecond. Images for t = 1 ms to 3 ms clearly show light emission from point locations where clumps of SWCNTs with Fe impurity have ignited, through the mechanisms discussed in references [1-4], and are emitting due to their oxidation in air. These clumps of photo-ignited SWCNTs are at temperatures around 1500 °C [1-4] allowing for the distributed thermal ignition of the ethylene/air mixture.

The hot glowing ignition points are distributed throughout the entire combustion chamber but appear to be of higher density in a central area of approximately half to two-thirds the diameter of the combustion chamber. However, within this central area the density of ignition points appears to be fairly homogeneous. This is probably due to the prerequisite power required for ignition of the SWCNTs in air, which Ajayan et al. [1] showed to be 100-300 $mWcm^{-2}$, and/or the distribution of SWCNTs following the injection process, which results in greater density in the central region of the chamber. Over the 1 ms flash duration the average flash power drops below 100 $mWcm^{-2}$ at a radius of approximately 16 mm, nearly two-thirds of the 25.4 mm chamber radius, supporting the inference that the distribution of the reaction zone is limited by flash output.

As time progresses the ethylene/air mixture reacts and ignites, due to the distributed hot spots, resulting in light emission. This emission is distributed throughout the chamber and is nearly homogeneous within a central region of approximately half to two-thirds the chamber diameter. Most importantly, no combustion wave propagation from the center of the chamber towards the wall is apparent in Figure A.4 and the gas emits and reacts in a quasi-homogeneous manner. Images filtered for electronically excited OH radical emission (not shown), although very weak in intensity, exhibited similar distributed emission and chemical reaction.

Camera images of unfiltered light emission for the traditional automotive spark ignition (105 mJ) of stoichiometric ethylene/air at an initial pressure of 1 bar were also obtained and can be found in Figure A.5. The spark ignition process is in stark contrast to the SWCNT photo-ignition process. The spark is fired at t = 0 resulting in an ignition kernel from which a spherical flame forms and propagates across the chamber. The spark ignition images (Figure A.5) show the flame front propagating across the combustion chamber from t = 1 ms to 5 ms and the light emission which results from chemical reaction

behind the flame front. In the spark ignition case, the requirement of flame front propagation for the consumption of the reactant mixture results in a longer ignition delay time, approximately 8 ms, in comparison to the quasi-homogeneous SWCNT photo-ignition, approximately 5 ms, as defined by pressure measurements. Note that the spark ignition images (Figure A.5) have been greatly enhanced through post-processing to capture the low luminosity from the flame front and spark, thus the grainer appearance of Figure A.5 compared to Figure A.4. Due to the enhancement of the spark ignition images, comparisons of the luminosity in Figures A.4 and A.5 are not indicative of the relative reaction progress or relative rate of energy release and cannot be directly compared for an indication of differences in these parameters. The measured ignition delay for the photo-ignition example (Figure A.4) is ~5ms, while that for the spark ignition example (Figure A.5) is ~8 ms.

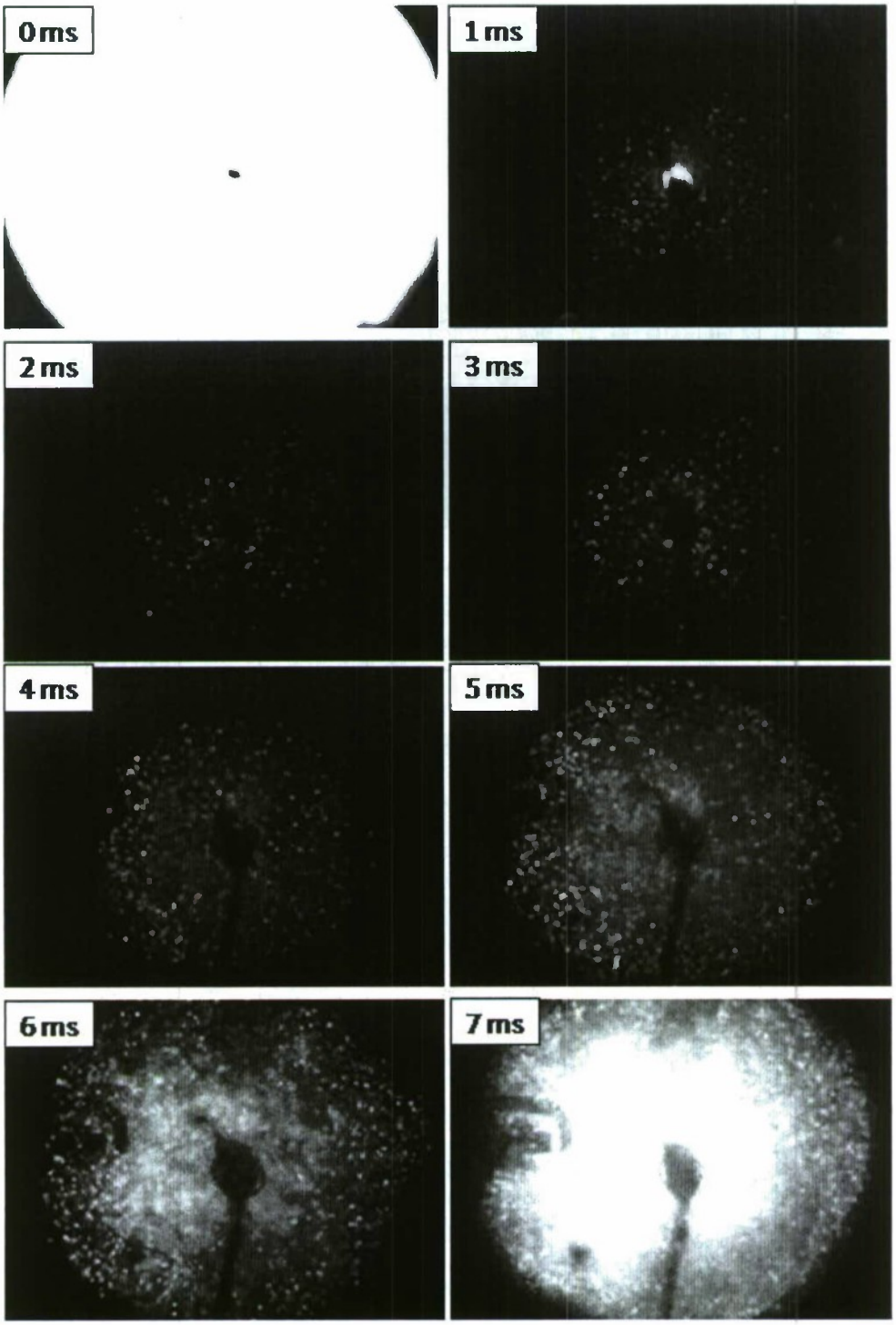

Figure A.4. High-speed images of the ignition process for the photo-ignition of SWCNTs containing Fe impurity at 70% by weight suspended in $\Phi = 1.0$ C_2H_4/air at an initial pressure of 1 bar. For this experiment the ignition delay time is approximately 5 ms.

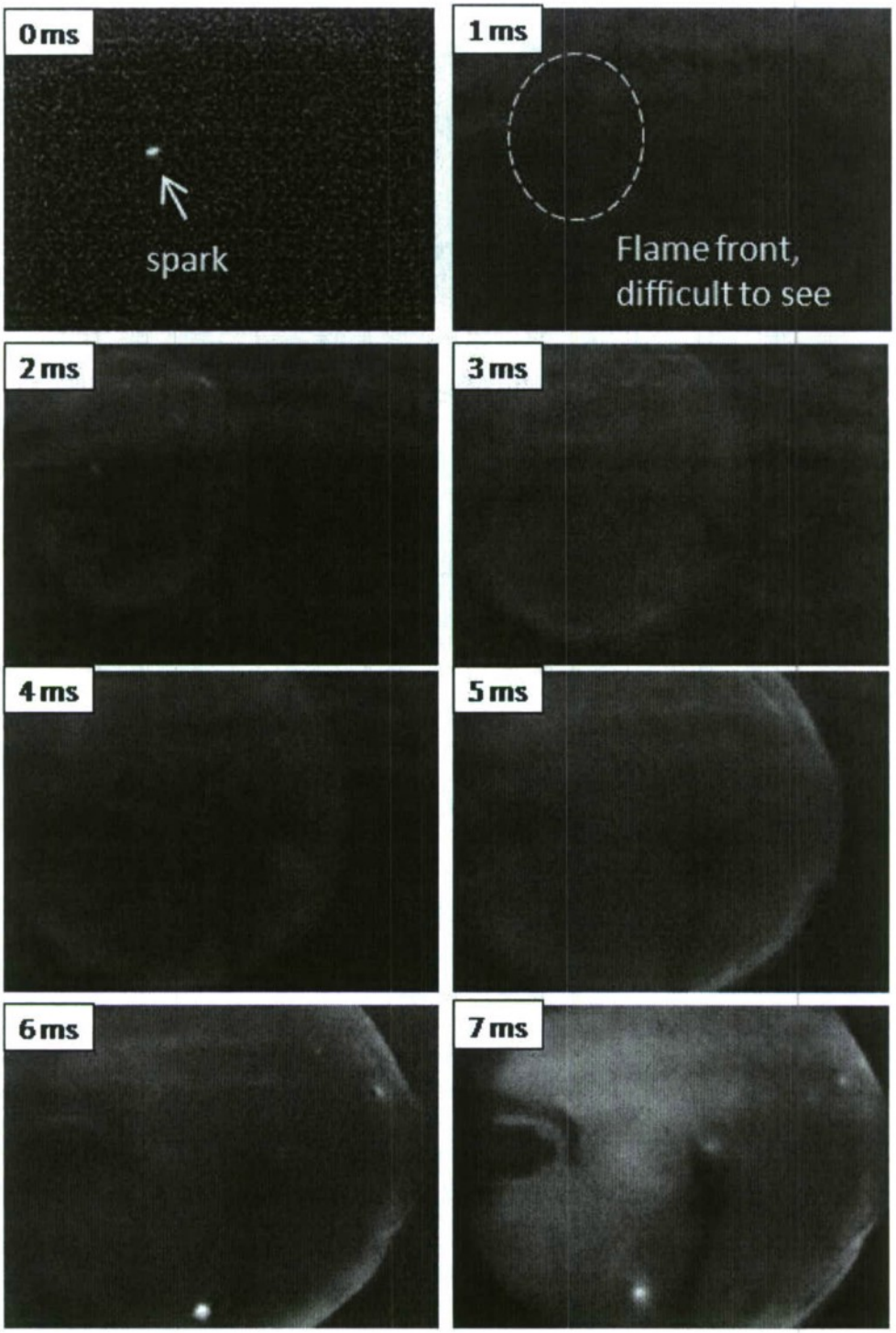

Figure A.5. High-speed images of the ignition process for the spark ignition (105 mJ) of $\Phi = 1.0$ C_2H_4/air at an initial pressure of 1 bar. For this experiment the ignition delay time is approximately 8 ms (at times longer than 7 ms the images simply grow more intense with little spatial variation).

b. Ignition delay and rise times

Measurements of ignition delay and rise times, based on measured dynamic pressure, were made for ethylene/air mixtures at equivalence ratios ranging from 0.5 to 1.5 and at initial pressures of 1 and 2 bar for both SWCNT photo-ignition and spark ignition (105 mJ). For reported photo-ignition experiments with variable equivalence ratio and pressure (this section), the mass of injected SWCNTs with 70% Fe impurity by weight was kept fixed at 2 mg. In Figure A.6 ignition delay and rise times for ethylene/air experiments at initial pressures of 1 and 2 bar are compared to spark ignition data obtained at the same conditions. For both spark and photo-ignition experiments the reproducibility (scatter) of ignition delay and rise time at a given pressure and equivalence ratio is around ±10-15%, this is exemplified in Figure A.7 discussed in the next section, and we estimate that the uncertainties are also around ±15%. The reproducibility/scatter in the ignition delay and rise data likely is mostly the result of shot-to-shot differences in SWCNT injection and dispersion and flash timing, which are crude in the current experimental apparatus. The uncertainties in initial pre-injection conditions are very small (±2% in equivalence ratio and pressure) and uncertainties in measured ignition rise or delay time for a given pressure measurement are also quite small (<±5%).

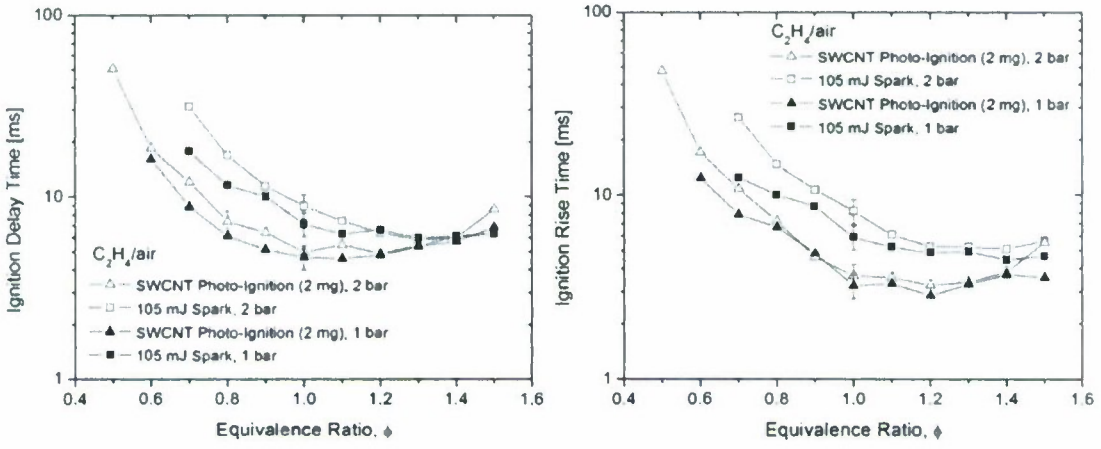

Figure A.6. Ignition delay and rise times for C_2H_4/air mixtures at initial pressures of 1 and 2 bar for SWCNT photo-ignition (2 mg of injected SWNCTs containing 70% Fe impurity by weight) and spark ignition (105 mJ).

The comparisons in Figure A.6 show that the ignition delay and rise times are significantly shorter for SWCNT photo-ignition in comparison to spark ignition at lean conditions but the advantages are reduced with increasing equivalence ratio. At $\Phi = 0.7$ the ignition delay and rise times are a factor of 2-3 shorter for photo-ignition compared to spark ignition and at $\Phi = 1.0$ the differences are a factor of 1.5-2. However, for $\Phi = 1.3$ and greater there is no discernible difference in the spark and photo-ignition ignition delay times and the differences in ignition rise times are a factor of 1.5 and smaller. The photo-

ignition process is dependent on the interaction of the Fe impurities imbedded in the SWCNTs with O_2 [4] and therefore the energy release rate for the photo-ignition of fuel/air mixtures is presumably less dependent on flame temperature than that for typical ignition processes. Hence, at leaner conditions, where flame temperature more dramatically falls off, the advantages of SWCNT photo-ignition compared to spark ignition are observed to be more dramatic.

It is important to point out that the absolute differences between the ignition delay and rise times for these two ignition processes are dependent on a number of other parameters not studied. As shown in the images, the spark ignition process is dependent on flame propagation and hence the ignition delay and rise times are dependent on the chamber volume and geometry. On the other hand, provided the SWCNTs containing Fe impurities can be distributed throughout a given combustion chamber volume and provided a light source of sufficient intensity, the SWCNT photo-ignition process should not be strongly dependent on chamber volume or geometry as it is a quasi-homogeneous process. Additionally, the absolute differences in the ignition delay and rise times for SWCNT photo-ignition and spark ignition are surely dependent on other variables not investigated here including spark energy and flash power and spectral characteristics.

From Figure A.6 it is evident that the differences in ignition delay and rise times are small, largely within the uncertainty limits, between the 1 and 2 bar data sets with both ignition delay and rise times slightly longer at 2 bar than at 1 bar for both ignition processes. These small differences can be understood via classical laminar flame speed analysis which specifies that the laminar flame speed decreases with increasing pressure due to the dependence of flame speed on diffusivities and overall reaction rate and the dependence of these on pressure [14]. The decrease in laminar flame speed with increasing pressure is also an experimental observation; for example ethylene/air laminar flame speed measurements at range of elevated pressures see Jomaas et al. [15]. In the case of the spark ignition, the ignition delay and rise time are governed, as is shown in the camera images, by the propagation of a spherical mostly laminar flame, due to the small size of the chamber, across the combustion chamber. Thus, the ignition delay and rise times for spark ignition, dependent on flame speed, increase with increasing pressure. Similarly, we hypothesize that the slightly longer ignition delay and rise times for the SWCNT photo-ignition at 2 bar in comparison to 1 bar are due to the increased diffusivities at the localized hot photo-ignition points. Although there is no observable macroscale reaction front propagation, the localized hot photo-ignition points are surrounded by quiescent room-temperature ethylene/air and thermal and species diffusion at these hot spots is important for formation of the first chemical reaction zones. Therefore, it is reasonable that there would also be a decrease in the rate of

growth of these first reaction zones and an increase, albeit very slight, in ignition delay and rise times for increasing pressure for SWCNT photo-ignition.

c. Dependence on injected/suspended mass

Experiments were performed to investigate the influence of the mass of injected nanotubes on ignition delay and rise times. The mass of injected SWCNTs with 70% Fe by weight was varied from 0.1 to 2 mg for photo-ignition experiments with stoichiometric ethylene/air at an initial pressure of 1 bar; see Figure A.7 for the results. The results show a slight decrease in ignition delay time with increasing injected SWCNT mass. However, even at an injection mass as low as 0.1 mg reliable ignition was observed with ignition delay times only 2 ms longer than those observed for 2 mg of injected SWCNTs. However, no dependence of ignition rise time, an indicator of heat release rate, was discernible with variation in the mass of injected SWCNTs from 0.1 to 2 mg. This is important because the heat release rate is likely to be more important, for the implementation of such a process into a practical combustion device, than the ignition delay, which can be adjusted through the timing of light illumination.

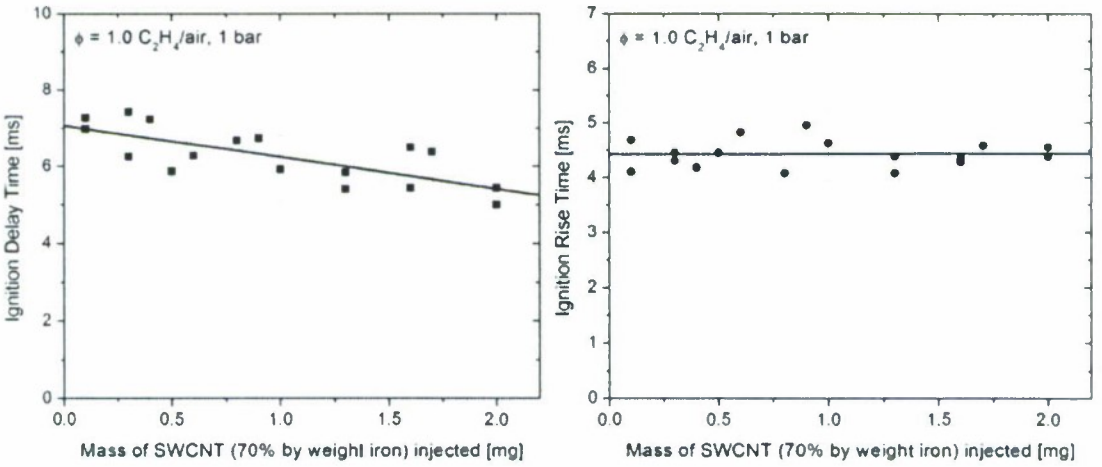

Figure A.7. Variation of ignition delay and rise times with mass of injected SWCNTs (70% Fe impurity by weight) for $\Phi = 1.0$ C_2H_4/air mixtures at an initial pressure of 1 bar.

Additionally, spark ignition experiments were performed with suspended SWCNTs to determine if the nanomaterial can influence the spark ignition and flame propagation processes. No discernible differences were observed in the dynamic pressure measurements and high-speed camera images for spark ignition with and without injected SWCNTs. Hence, we are safe in the assumption that the above observations regarding the SWCNT photo-ignition process are indeed unique to the photo-induced ignition and not the result of the modification of a flame propagation process by the suspended

nanomaterials. Also, to ensure that there was no charge leakage from the flash circuit which could generate a spark inside the combustion chamber, it was verified that ignition does not occur when ethylene/air mixtures without suspended SWCNTs were exposed to the Xe camera flash.

A.4. Summary

Here the photo-induced ignition of quiescent fuel/air mixtures containing suspended photo-sensitive nanomaterials has been demonstrated. Single wall carbon nanotubes (SWCNTs) with 70% Fe impurity by weight were suspended in ethylene/air mixtures in a static combustion chamber and exposed to a camera flash to cause ignition of the mixture. For comparison, traditional automotive spark ignition experiments were also carried out for ethylene/air mixtures. High-speed camera images show that SWCNT photo-ignition process results in distributed quasi-homogeneous ignition and the consumption of the fuel/air mixture without the formation of a discernible combustion wave. This is in stark contrast to spark ignition, which results in a single ignition kernel and spherical flame propagation across the combustion chamber. Dynamic pressure measurements illustrate that the SWCNT photo-ignition provides a more rapid rise in pressure and higher peak pressures, which corresponds to shorter ignition delay and rise times, than spark ignition. Additionally, the photo-ignition process can be implemented for relatively small amounts of injected and suspended SWCNTs containing Fe impurities, can occur for relatively low levels of light exposure (100-300 mW/cm^2), and can be performed using a very inexpensive and simple light source, such as the Xe camera flash used in this study. The photo-ignition method may prove to have potential in a variety of combustion and propulsion applications where the ability to reliably ignite and burn combustible mixtures on demand and with greater distribution could improve performance.

A.5. References

1. P.M. Ajayan, M. Terrones, A. de la Guardia, V. Huc, N. Grobert, B.Q. Wei, H. Lezec, G. Ramanath, T.W. Ebbesen, Science 296, 705 (2002).
2. B. Bockrath, J.K. Johnson, D.S. Sholl, B. Howard, C. Matranga, S. Wei, D. Sorescu, Science 297, 192 (2002).
3. N. Braidy, G.A. Botton, A. Adronov, Nano Lett. 2, 1277 (2002).
4. J. Smits, B. Wincheski, M. Namkung, R. Crooks, R. Louie, Mat. Sci. Eng. A 358, 384 (2003).
5. J. Huang, R.B. Kaner, Nat. Mater. 3 783 (2004).
6. S. Singamaneni, V. Shevchenko, V. Bliznyuk, Carbon 44, 2191 (2006).
7. S.H. Tseng, N.H. Tai, W.K. Hsu, L.J. Chen, J.H. Wang, C.C. Chiu, C.Y. Lee, L.J. Chou, K.C. Keou, Carbon 45, 958 (2007).
8. B. Kang, Y. Dai, S. Chang, D. Chen, Carbon 46, 974 (2008).

9. B. Chehroudi, S.A. Danczyk, A Novel Distributed Ignition Method Using Single-Wall Carbon Nanotubes (SWCNTS) and a Low-Power Flash Light, Global Powertrain Congress – World Powertrain Exposition, 2006.
10. B. Chehroudi, G.L. Vaghjiani, A.D. Ketsdever, Method for Distributed Ignition of Fuels by Light Sources, U.S. Patent 7,517,215 B1, April 14, 2009.
11. B. Chehroudi, G.L. Vaghjiani, A.D. Ketsdever, Apparatus for Distributed Ignition of Fuels by Light Sources, U.S. Patent 7,665,985 B1, February 23, 2010.
12. M.R. Manaa, A.R. Mitchell, R.G. Garza, P.F. Pagoria, B.E. Watkins, J. Am. Chem. Soc. 127, 13796 (2005).
13. F. Wang, J.B. Liu, J. Sinibaldi, C. Borphy, A. Kuthi, C. Jiang, P. Ronney, M.A. Gundersen, IEEE Trans. Plasma Sci. 33, 844 (2005).
14. K.K. Kuo, "Principles of Combustion, Second Edition," John Wiley and Sons, Hoboken, New Jersey (2005).
15. G. Jomaas, X.L. Zheng, D.L. Zhu, C.K. Law, Proc. Combust. Inst. 30, 193 (2005).